

# Thin film epitaxial [111] Co<sub>50</sub>Pt<sub>50</sub>: Structure, magnetisation, and spin polarisation

N. Satchell<sup>1</sup>, S. Gupta<sup>1</sup>, M. Maheshwari<sup>1</sup>, P. M. Shepley<sup>1</sup>, M. Rogers<sup>1</sup>, O. Cespedes<sup>1</sup>, and G. Burnell<sup>1,\*</sup>

<sup>1</sup>School of Physics and Astronomy, University of Leeds, Leeds, LS2 9JT, United Kingdom

\*g.burnell@leeds.ac.uk

## ABSTRACT

Ferromagnetic films with perpendicular magnetic anisotropy are of interest in spintronics and superconducting spintronics. Perpendicular magnetic anisotropy can be achieved in thin ferromagnetic multilayer structures, when the anisotropy is driven by carefully engineered interfaces. Devices with multiple interfaces are disadvantageous for our application in superconducting spintronics, where the current perpendicular to plane is affected by the interfaces. Robust intrinsic PMA can be achieved in certain Co<sub>x</sub>Pt<sub>100-x</sub> alloys and compounds at any thickness, without increasing the number of interfaces. Here, we grow equiatomic Co<sub>50</sub>Pt<sub>50</sub> and report a comprehensive study on the structural, magnetic, and spin-polarisation properties in the  $L1_1$  and  $L1_0$  ordered compounds. Primarily, interest in Co<sub>50</sub>Pt<sub>50</sub> has been in the  $L1_0$  crystal structure, where layers of Pt and Co are stacked alternately in the [100] direction. There has been less work on  $L1_1$  crystal structure, where the stacking is in the [111] direction. For the latter  $L1_1$  crystal structure, we find magnetic anisotropy perpendicular to the film plane. For the former  $L1_0$  crystal structure, the magnetic anisotropy is perpendicular to the [100] plane, which is neither in-plane or out-of-plane in our samples. We obtain a value for the ballistic spin polarisation of the  $L1_1$  and  $L1_0$  Co<sub>50</sub>Pt<sub>50</sub> to be  $47 \pm 3\%$ .

## Introduction

Ferromagnetic films with perpendicular magnetic anisotropy (PMA) are of wide interest for applications in established and nascent technologies such as ultrahigh density magnetic hard drives<sup>1</sup>, MRAM<sup>2</sup>, superconducting spintronics<sup>3</sup>, and energy efficient spin-orbit torque memory<sup>4</sup>. PMA can be achieved in Pt/Co/Pt multilayer systems as a result of the interfacial anisotropy, however at a critical Co thickness, typically about 1 nm, the anisotropy will fall in-plane. Increasing the total ferromagnetic layer thickness further therefore involves adding additional interfaces to the multilayer. Having a multilayer structure introduces interfacial resistance and interfacial spin-flip scattering<sup>5</sup>, which are disadvantageous for applications such as ours which require the transport current perpendicular-to-plane<sup>6-8</sup>. Alternately, robust intrinsic PMA can be achieved in certain Co<sub>x</sub>Pt<sub>100-x</sub> alloys and compounds at any thickness, without increasing the number of interfaces.

Here, we study the equiatomic Co<sub>50</sub>Pt<sub>50</sub> alloy, hereafter referred to as CoPt. Through growth at elevated temperatures it is possible to form the  $L1_1$  and  $L1_0$  chemically ordered compounds of CoPt as epitaxial films. Previous experimental studies of such compounds tend to use MgO substrates as the basis for high temperature epitaxial growth. Visokay and Sinclair report  $L1_0$  crystal structure on MgO [001] substrates for growth temperatures above 520°C<sup>9</sup>. Iwata *et al.* report growth of  $L1_1$  crystal structure on MgO [111] substrates for a growth temperature of 300°C<sup>10</sup>.

Early thin film studies of the chemically ordered CoPt (and the related FePt and FePd) compounds were motivated by the large out-of-plane anisotropy and narrow domain wall widths being candidate for high density storage mediums<sup>9-53</sup>. Recently, renewed interest in these compounds has been driven by the discovery of self-induced spin-orbit torque switching in these materials, which can be used as the switching mechanism for a low-dissipation magnetic memory<sup>54-61</sup>.

Our motivation for studying [111] CoPt is to incorporate this PMA ferromagnet in an all epitaxial heterostructure suitable for superconducting Josephson devices<sup>6-8</sup> or MRAM<sup>2</sup>. For these applications growth in the [111] direction is favourable. In Josephson junctions, the superconductor of choice is Nb, which can be grown epitaxially as a bcc structure in the [110] direction<sup>62</sup>. In MRAM, the seed layer of choice is Ta, which has almost identical structural properties to Nb. On Ta or Nb [110] layers, we know that Pt and Co will grow with [111] orientation<sup>63</sup>. We therefore choose Al<sub>2</sub>O<sub>3</sub> [0001] substrates for this study and use thin Pt [111] seed layers to grow CoPt [111]<sup>37</sup>. As far as we are aware, no previous works have reported the properties of [111] ordered films of  $L1_0$  and  $L1_1$  CoPt on Al<sub>2</sub>O<sub>3</sub> [0001] substrates. We are also unaware of any measurements of the spin polarisation of CoPt.

We fabricate and report the properties of three sets of samples. The first set is designed to determine the optimal growth temperature. Therefore, we fix the thickness  $d_{CoPt} = 40$  nm and vary the substrate heater temperature in the range from 27°C to

850°C. The next two sample sets are thickness series grown by varying the growth time at a fixed temperature and magnetron powers. The temperatures chosen for the thickness series are to produce either the  $L1_1$  (350°C) or  $L1_0$  (800°C) crystal structures. These temperatures are guided by the results of the first temperature series of samples. Thicknesses are varied over the range  $1 \text{ nm} \leq d_{\text{CoPt}} \leq 128 \text{ nm}$ .

On each sample set we report systematically on the structural and magnetic properties of the CoPt. Additionally, on the thickest 128 nm  $L1_1$  and  $L1_0$  samples we perform point contact Andreev reflection (PCAR) measurements with a Nb tip at 4.2 K to determine the spin polarisation. The use of Nb as the tip, the temperature of this measurement, and the ballistic transport regime probed are relevant for our proposed application of the CoPt in Josephson devices<sup>6–8</sup>.

## Results and Discussion

### CoPt properties as a function of growth temperature

We expect that as the growth temperature is increased the CoPt will form initially a chemically disordered A1 alloy phase, followed by a chemically ordered  $L1_1$  crystal structure, an intermediate temperature A1 phase, and finally a chemically ordered  $L1_0$  crystal structure respectively. In order to map out the growth parameters we report on  $\text{Al}_2\text{O}_3(\text{sub})/\text{Pt}(4 \text{ nm})/\text{CoPt}(40 \text{ nm})/\text{Pt}(4 \text{ nm})$  sheet films grown at different set temperatures in the range from room temperature (RT) to 850°C.

#### Structure

In order to understand the magnetic phases of sputter deposited CoPt, it is necessary to understand the underpinning structure and the influence of the growth temperature. Therefore, the structural characteristics and film quality were investigated using x-ray diffraction (XRD) as a function of growth temperature. Fig. 1 (a-c) shows the acquired XRD for selected growth temperatures around the main CoPt [111] structural peak. Further XRD data are available in the Supplemental Information online. The CoPt [111] structural peak is clearly observable for all growth temperatures. The presented data at growth temperatures of 350°C and 800°C show additional Pendellosung fringes which bracket the primary CoPt [111] peak. The CoPt [111] relative peak intensity is shown as a function of growth temperature in Fig. 1 (d). In Fig. 1 (a), for a growth temperature of 350°C, the additional feature at  $2\theta \approx 40^\circ$  corresponds to the superimposed Pendellosung fringes and the Pt [111] structural peak (bulk Pt has a lattice constant of 3.92Å). This additional Pt structural peak is present for growths up to 550°C (see Supplementary Information online) which is within the expected optimal temperature range for sputter deposited Pt films on  $\text{Al}_2\text{O}_3$ <sup>64</sup>. To maintain consistent Pt structure for CoPt growths at different temperatures, future work could grow the Pt layer at its optimum growth temperature.

Using the Scherrer equation and the full widths at half maxima of the Gaussian fits to the CoPt [111] structural peaks, an estimation of the CoPt crystallite sizes can be made. The crystallite size determined by the main [111] structural peak is given in Fig. 1 (e). In the expected range of the ordered  $L1_1$  crystal structure between 200°C and 400°C, the estimated CoPt crystallite size is 37 nm, which compared to the nominal thickness of 40 nm indicates that the CoPt has high crystallinity. On the other hand, at RT growth and intermediate temperatures between 400°C and 800°C, the estimated CoPt crystallite size is much lower, showing a minimum value of 22 nm at 700°C where we expect A1 growth. Interestingly, the disorder in the A1 growth appears to affect both the chemical disorder (random positions of the Co and Pt atoms in the unit cell) and leads to a poorer crystallite size compared to the chemically ordered crystal structures. The disappearance of the Pendellosung fringes at these intermediate growth temperatures is related to the increased roughness of the A1 films. Finally, upon increasing the temperature further to 800°C and 850°C the crystallite size reaches a maximum of 49 nm. This value corresponds approximately to the entire thickness of the Pt/CoPt/Pt trilayer, indicating that the Pt buffer and capping layers have fully interdiffused into the CoPt layer.

Fig. 1 (f) shows the CoPt  $c$ -plane space calculated from the center of the fitter Gaussian to the main [111] structural peak. At all temperatures the measured  $c$ -plane spacing is very close to the expected value based on single crystal studies<sup>65</sup>, indicating low out-of-plane strain. The trend with temperature, however, is non-monotonic and shows a discrete increase between the samples grown at 550°C and 650°C. The transition associated with the  $L1_0$  crystal structure is expected to result in a transition from cubic to tetragonal crystal with a  $c/a = 0.979$  in the single crystal<sup>65</sup>. In the single crystal study, however, the  $c$ -axis is in the [001] orientation. In our [111] orientated film, the small structural transition from cubic to tetragonal crystal structure is not expected to be visible in the [111] peak studied here. Nonetheless, Fig. 1 (f) shows features consistent with the CoPt undergoing structural transitions.

X-ray reflectivity (XRR) is performed to further investigate the growth temperature dependent trends in the structural properties of the films. Fig. 2 (a,c,e) show the low angle XRR for selected growth temperatures along with the best fits to the data. The corresponding models are shown in Fig. 2 (b,d,f). Further XRR data are available in the Supplemental Information online. The fitting is performed using the GenX package<sup>66</sup>, which models each layer as a box with independent thickness, roughness, and density fitting parameters. Across 13 samples grown at varying temperatures, the average total sample thickness is  $47.2 \pm 0.3 \text{ nm}$ , compared to a nominal total thickness of 48.0 nm, confirming the sputter rate calibration and that the growth temperature has not impacted the growth rate. For growth temperatures of 450°C and below, the XRR is best modelled as a

Pt/CoPt/Pt trilayer, for example Fig. 2 (a,b). At a growth temperature of 550°C and above there is a clear change in the XRR. Modelling the data suggests that the interdiffusion has become so large that a trilayer model is no longer required. For the data shown in Fig. 2 (c-f), a single layer model is used to fit the reflectivity.

Fig. 2 (g) shows the extracted roughness parameter on the top surface of the sample. The surface roughness shows temperature dependence corresponding to the underpinning structure of the CoPt film. For the optimal growth temperature to achieve the  $L1_1$  crystal structure, the corresponding surface roughness is lowest. In the A1 growth regime, the disorder in the crystal structure evident in the XRD is also present in the film surface roughness. The lower roughness is recovered at higher temperatures at the optimal growth temperature for the  $L1_0$  crystal structure. Fig. 2 (h) shows an extracted interfacial roughness parameter at the CoPt/Pt interface. We interpret this parameter as a measure of the interdiffusion between the layers. As expected, a clear trend is present where the interdiffusion between the layers increases with increasing temperatures. At the highest growth temperatures where a single layer model is used to fit the data, there is no interfacial roughness parameter to extract as the layer has completely interdiffused.

### Magnetic characterisation

The magnetisation versus field data are shown in Fig. 3 for  $\text{Al}_2\text{O}_3(\text{sub})/\text{Pt}(4\text{ nm})/\text{CoPt}(40\text{ nm})/\text{Pt}(4\text{ nm})$  sheet film samples. Further magnetisation data for all samples in this study are available in the Supplemental Information online. The 350°C, 550°C, and 800°C samples are plotted here as they are representative of the magnetic response of the  $L1_1$  crystal structure, the chemically disordered A1 phase, and  $L1_0$  crystal structure respectively. Magnetisation is calculated from the measured total magnetic moments, the areas of the sample portions, and the nominal thicknesses of the CoPt layer.

For the chemically ordered  $L1_1$  crystal structure shown in Fig. 3 (a), the OOP hysteresis loop shows a wasp waisted behavior associated with the formation of magnetic domains at remanence. Such behavior is common in CoPt alloys and multilayer thin films<sup>9</sup>. The wasp waisted OOP hysteresis loop along with the low IP remanence and higher IP saturation field indicates that the 40 nm CoPt samples with the  $L1_1$  crystal structure have strong PMA. We can estimate the effective anisotropy using the expression  $K_{\text{eff}} = \mu_0 M_s H_s / 2$ , where  $\mu_0$  is the vacuum permeability,  $M_s$  the saturation magnetisation, and  $H_s$  is the saturation magnetic field. We estimate from the hysteresis loop that  $H_s$  in-plane is 0.8 T (based on when the magnetisation reaches 97.5% of the fitted saturation value), and therefore  $K_{\text{eff}} = 0.4 \pm 0.1 \text{ MJ/m}^3$ . The effective anisotropy includes the uniaxial and shape anisotropy.

For samples grown at intermediate temperatures with the chemically disordered A1 structure, the magnetism favours IP anisotropy at 40 nm, shown for growth at 550°C in Fig. 3 (b).

For the chemically ordered  $L1_0$  crystal structure shown in Fig. 3 (c), there is a significant increase in the coercivity and squareness ratio ( $M_r/M_s$ ) for both the IP and OOP field orientations. The increased coercive field suggests that the  $L1_0$  CoPt is magnetically hard compared to the  $L1_1$  and A1 samples. The magnetisation of the  $L1_0$  40 nm CoPt sample does not show clear IP or OOP anisotropy from these measurements.

The magnetisation vs growth temperature is shown in Fig. 3 (d). At growth temperatures below 550°C the magnetisation remains approximately constant, however at higher temperatures the magnetisation begins to decrease with increasing temperature. The possible cause of this decrease is the higher growth temperature contributing to interdiffusion between the Pt and CoPt layers, creating magnetic dead layers.

The saturation field and squareness ratio vs growth temperature are shown in Fig. 3 (e) and (f) respectively. The general trends can be seen in the differences observed in the hysteresis loops of Fig. 3 (a-c). These trends allow us to characterise the growth temperatures corresponding to the different crystal growths in our samples, further supporting our conclusions from the XRD: the  $L1_1$  crystal structure driving the magnetic response of samples grown from 200°C to 400°C, the  $L1_0$  crystal structure for samples grown above 750°C, and the intermediate temperatures being the chemically disordered A1 phase.

In the  $L1_0$  crystal structure, Fig. 3 (c), the high squareness ratio for both field orientations suggests that the anisotropy axis of the material is neither parallel or perpendicular to the film. Instead, it is possible that the magnetic anisotropy is perpendicular to the layer planes, which are stacked in the [100] direction.

To further investigate the anisotropy, we pattern our  $L1_1$  350°C and  $L1_0$  800°C samples into Hall bars and perform angular dependent Hall resistivity,  $R_{xy}(\theta)$ , measurements, Fig 4. The fabricated Hall bar and measurement geometry is shown in Fig 4 (a).  $R_{xy}(\theta)$  for the  $L1_1$  350°C and  $L1_0$  800°C Hall bars are shown in Fig 4 (b) and (c) respectively. For the  $L1_1$  350°C sample with out-of-plane anisotropy,  $R_{xy}(\theta)$  shows a plateau close to out-of-plane field and a uniform response for angles in between. The plateau is interpreted as an angle forming between the magnetisation and applied field because of the anisotropy axis<sup>67</sup>. In comparison, the  $L1_0$  800°C sample also shows a  $R_{xy}(\theta)$  plateau for out-of-plane applied field plus an additional plateau for applied field angles between about 45° and 60°. We interpret the additional plateau in  $R_{xy}(\theta)$  for the  $L1_0$  800°C CoPt sample as evidence for an additional anisotropy axis, which we propose is perpendicular the [100] direction. The [100] plane has a dihedral angle of 54.75° with the [111] growth plane. Additional sources of anisotropy in our samples are interface anisotropy at the Pt/CoPt interfaces, which would favour out-of-plane magnetisation for thin layers, and shape anisotropy, which for our thin films would favour in-plane magnetisation.

Fig. 5 shows the extracted coercive field as a function of in-plane rotator angle for the  $L1_0$  800°C sample. The data shows a clear six-fold symmetry. This is consistent with an easy axis for the plurality tetragonal  $L1_0$  phase of [001] when grown on {111} planes - the  $\langle 100 \rangle$  directions of the parent cubic structure are inclined at  $\pm 45^\circ$  from the plane and are coupled with the three fold symmetry of {111}. The magnetometry data therefore strongly suggests that over the sample the [001] $_{L1_0}$  can be found in any of the three possible  $\langle 100 \rangle$  of the parent cubic structure without a strong preference for which of the possible twins grow.

### CoPt properties as a function of thickness for $L1_1$ and $L1_0$ crystal structures

Having obtained optimal growth conditions for CoPt with chemically ordered  $L1_1$  and  $L1_0$  crystal structures, in this section, we report on the properties of samples  $\text{Al}_2\text{O}_3$  (sub)/Pt (4 nm)/CoPt ( $d_{\text{CoPt}}$ )/Pt (4 nm) with  $d_{\text{CoPt}}$  varied between 1 nm and 128 nm for both the  $L1_1$  and  $L1_0$  crystal structures.

#### Magnetisation of $L1_1$ and $L1_0$ CoPt

The hysteresis loops for  $\text{Al}_2\text{O}_3$ (sub)/Pt(4 nm)/CoPt(4 nm)/Pt(4 nm) sheet films is shown in Fig. 6 (a) and (b) for the  $L1_1$  (350°C) and  $L1_0$  (800°C) crystal structures respectively. Hysteresis loops over the full thickness range are given in the Supplementary Information online. The moment/area at saturation (or 6 T) versus nominal CoPt thickness are presented in Fig 6 (c) and (d).

We calculate the magnetisation ( $M$ ) by fitting the moment/area versus nominal CoPt thickness data. In order to account for interfacial contributions to the magnetisation of the CoPt, we model the system as a magnetic slab with possible magnetic dead layers and/or polarised adjacent layers. Magnetic dead layers can form as a result of interdiffusion, oxidation, or at certain interfaces with non-ferromagnetic layers. At some ferromagnet/non-ferromagnet interfaces, the ferromagnetic layer can create a polarisation inside the non-ferromagnetic layer by the magnetic proximity effect. Polarisation is particularly common at interfaces with Pt<sup>68–72</sup>. To take these into account, we fit to the expression,

$$\text{moment/area} = M(d_{\text{CoPt}} - d_i), \quad (1)$$

where  $d_i$  is the contribution to  $M$  from any magnetic dead layers or polarisation. The resulting best fit and the moment/area versus the nominal CoPt thickness is shown in Fig. 6.

For  $L1_1$  growth at 350°C, the result of fitting Eqn. 1 shown in Fig. 6 (c) gives  $M = 750 \pm 50 \text{ emu/cm}^3$  and  $d_i = 0.38 \pm 0.05 \text{ nm}$ . From the XRR data and fitting presented in Fig. 2, the interdiffusion of the Pt seed and capping layers and the CoPt layer is minimal at this growth temperature, which is consistent with the small dead layer  $d_i$ .

For  $L1_0$  growth at 800°C, the thinnest 1 nm and 2 nm films did not display any magnetic response and are excluded from the analysis in Fig. 6. This suggests the formation of a magnetic dead layer or alternatively a large enough change to the stoichiometry that those films were no longer magnetic. From the XRR data and fitting presented in Fig. 2, there is significant interdiffusion between the Pt seed and capping layers and the CoPt. The result of fitting Eqn. 1 shown in Fig. 6 (d) for the samples thicker than 2 nm gives  $M = 520 \pm 50 \text{ emu/cm}^3$  and  $d_i = -2 \pm 1 \text{ nm}$ . Interestingly, we find a significant difference in  $M$  between the two crystal structures, which is consistent with a previous report of CoPt growth on MgO substrates<sup>43</sup>. It is possible that the differences in  $M$  corresponds to a true difference in the saturation magnetisation of the two crystal structures. An alternative scenario is that the 6 T applied field is not large enough to fully saturate the  $L1_0$  samples, leading to a reduced measured  $M$ . Another possibility is that the interdiffusion of the Pt seed and capping layers during growth at 800°C modifies the stoichiometry of the resulting  $L1_0$  film, and hence reduces the magnetisation.

The thickness dependence of the magnetic switching of the  $L1_1$  samples is well summarised by the squareness ratio shown in Fig 6 (e). The thickest 40 and 128 nm samples are wasp waisted, as presented in Fig. 3. At reduced thicknesses, between 2 and 8 nm, the  $L1_1$  CoPt no longer displays the wasp waisted switching for out-of-plane field orientation, and now has a square loop shown in Fig. 6 (a). The 16 nm sample showed an intermediate behaviour. At 1 nm, the magnetic switching showed "S" shaped hysteresis loops for both in- and out-of-plane applied fields with small remanent magnetisation, see Supplementary Information online.

The thickness dependence of the  $L1_0$  crystal structure samples is significantly different to the  $L1_1$ . In the thinnest films of 1 and 2 nm there is no evidence of ferromagnetic ordering in the hysteresis loops, see Supplementary Information online. For  $L1_0$  growth at 800°C, the XRR measurements (Fig. 2) suggests interdiffusion at the Pt/CoPt interfaces during high growth temperature. The interdiffusion may account for magnetic dead layers, which in the thinnest samples may prevent ferromagnetic ordering. Upon increasing the thickness to 4 nm, a ferromagnetic response was recovered, however the hysteresis loops and extracted squareness ratio (Fig. 6) (f)) indicate that the 4 nm and 8 nm  $L1_0$  samples have in-plane magnetisation. The in-plane magnetisation in the thinner films suggests that the long-range  $L1_0$  ordering may have not established at those thicknesses.

The thickness dependence in both crystal structures suggest that the Pt/CoPt/Pt trilayers grown on  $\text{Al}_2\text{O}_3$  substrates are not suitable for applications where ultrathin magnetic layers are required. To improve the magnetic properties of the thinnest samples in this study our future work will focus on replacing the Pt layers with seed and capping layers where interdiffusion may be less.



## Spin polarisation

To estimate the spin polarisation in the chemically ordered  $L1_0$  and  $L1_1$  CoPt samples, we perform Point Contact Andreev Reflection (PCAR) spectroscopy experiments<sup>30,36,73–76</sup>. In the PCAR technique, spin polarisation in the ballistic transport regime can be determined from fitting the bias dependence of the conductance with the a modified Blonder-Tinkham-Klapwijk (BTK) model<sup>77</sup>.

We measure the  $\text{Al}_2\text{O}_3(\text{sub})/\text{Pt}(4\text{ nm})/\text{CoPt}(128\text{ nm})/\text{Pt}(4\text{ nm})$  samples grown at  $350^\circ\text{C}$ , corresponding to  $L1_1$  crystal structure, and  $800^\circ\text{C}$ , corresponding to  $L1_0$  crystal structure. The PCAR experiment was performed with a Nb wire tip at 4.2 K. Exemplar conductance spectra with fits to the BTK model are given in Fig. 7 (a). The interpretation of PCAR data is rife with difficulties<sup>78</sup> and a common issue with the PCAR technique is the presence of degenerate local fitting minima. To ensure that a global best fit is obtained, the fitting code makes use of a differential-evolution algorithm and we then consider the spin polarisation and barrier strength parameter for a large number of independent contacts to the same sample.

Fig. 7 (c) shows the dependence of the polarisation as a function of the square of the barrier strength,  $Z^2$ . The dashed lines in Fig. 7 are linear fits to the data. The value of the true spin polarisation is often taken to correspond to  $Z = 0$ , however this is strictly nonphysical. Nevertheless, in an all metal system it is possible to produce contacts approaching an ideal case and extrapolating to  $Z = 0$  is close to the (finite) minimum. We find that  $P = 47 \pm 3\%$  for both  $L1_1$  and  $L1_0$  CoPt samples. This compares to  $\approx 42\%$  for  $L1_0$  FePt<sup>30</sup> and  $\approx 50\%$  for  $L1_0$  FePd<sup>36</sup>.

## Conclusions

The major conclusions of this work may be summarised as follows. On  $c$ -plane  $\text{Al}_2\text{O}_3$  with thin Pt [111] buffer layers, the  $\text{Co}_{50}\text{Pt}_{50}$  grows following the [111] ordering. Through growth at elevated temperatures,  $\text{Co}_{50}\text{Pt}_{50}$  is grown epitaxially in the chemically ordered  $L1_1$  and  $L1_0$  crystal structures or the chemically disordered A1 phase. The  $L1_1$   $\text{Co}_{50}\text{Pt}_{50}$  grown between  $200^\circ\text{C}$  and  $400^\circ\text{C}$  shows perpendicular magnetic anisotropy for thicknesses  $\geq 2\text{ nm}$ . The  $L1_0$   $\text{Co}_{50}\text{Pt}_{50}$  grown above  $800^\circ\text{C}$  shows significantly harder magnetic anisotropy, which is perpendicular to the [100] direction for thicknesses  $\geq 40\text{ nm}$ . For growth at intermediate temperatures,  $450 < 800^\circ\text{C}$ , the  $\text{Co}_{50}\text{Pt}_{50}$  shows a disordered structure and in-plane magnetic anisotropy associated with the A1 phase. At growth temperatures of  $550^\circ\text{C}$  and above, significant interdiffusion between the CoPt and the Pt seed and capping layers is observed. The spin-polarisation of the  $L1_1$  and  $L1_0$   $\text{Co}_{50}\text{Pt}_{50}$  is determined by the PCAR technique to be  $47 \pm 3\%$ .

## Methods

### Epitaxial growth

Samples are dc sputter deposited in the Royce Deposition System<sup>79</sup>. The magnetrons are mounted below, and confocal to, the substrate with a source-substrate distance of 134 mm. The base pressure of the vacuum chamber is  $1 \times 10^{-9}$  mbar. The samples are deposited at elevated temperatures, with an Ar (6N purity) gas pressure of  $4.8 \times 10^{-3}$  mbar.

For alloy growth, we use the co-sputtering technique. To achieve as close to a  $\text{Co}_{50}\text{Pt}_{50}$  stoichiometry as possible, first, single layer samples of Co or Pt are grown at room temperature on  $10 \times 10\text{ mm}$  thermally oxidised Si substrates varying the magnetron power. From this initial study, it is found that a growth rate of  $0.05\text{ nm s}^{-1}$  is achieved for a Co power of 45W and a Pt power of 25W. These growth powers are fixed for the rest of the study.

For the growth of the CoPt samples,  $20 \times 20\text{ mm}$   $c$ -plane sapphire substrates are used. The substrates are heated by a ceramic substrate heater mounted directly above the substrate holder. The measured substrate heater temperature is reported. We note that the temperature on the substrate surface is most likely to be below the reported heater temperature. The substrate heater is ramped up from room temperature to the set temperature at a rate of  $3\text{--}5^\circ\text{C min}^{-1}$ . Once at the set temperature, the system is given 30 min to reach equilibrium before starting the sample growth.

Once the system is ready for growth, 4 nm Pt seed layer is deposited. The seed layer is immediately followed by the CoPt layer, which is deposited at a rate of  $0.1\text{ nm s}^{-1}$  by co-sputtering from the two targets at the determined powers. Finally, a 4 nm Pt capping layer is deposited to prevent the samples from oxidising. The final sample structure is  $\text{Al}_2\text{O}_3(\text{sub})/\text{Pt}(4\text{ nm})/\text{CoPt}(d_{\text{CoPt}})/\text{Pt}(4\text{ nm})$ . Following deposition, the samples are post growth annealed for 10 min at the growth temperature before the substrate heater is ramped down to room temperature at  $10^\circ\text{C min}^{-1}$ .

### Characterisation

Magnetisation loops are measured using a Quantum Design MPMS 3 magnetometer. Angular dependent magnetization measurements are performed using the Quantum Design Horizontal Rotator option. X-ray diffraction and reflectivity is performed on a Bruker D8 diffractometer with an additional four-bounce monochromator to isolate Cu K- $\alpha$  at a wavelength of  $1.5406\text{ \AA}$ . Sheet films are patterned into Hall bars of  $5\text{ }\mu\text{m}$  width using conventional photolithography and Ar ion milling.

Resulting devices are measured using 4-point-probe transport to measure the Hall resistance of the films using a combined Keithley 6221-2182A current source and nano-voltmeter.

## PCAR

Our experimental setup for performing PCAR measurements is described elsewhere<sup>30,36,74–76</sup>. The Nb tips are prepared from commercial 99.9% pure Nb wires with a diameter of 0.5 mm. An AC lock-in detection technique using Stanford Research Systems SR830 lock-in amplifiers is used for the differential conductance measurements. The tip position is mechanically adjusted by a spring-loaded rod driven by a micrometer screw. The experiment is carried out in liquid He at a fixed temperature of 4.2 K and at zero applied magnetic field.

## Availability of Data and Materials

The datasets generated and/or analysed during the current study are available in the University of Leeds repository, <https://doi.org/10.5518/1275>.

## References

1. Piramanayagam, S. N. Perpendicular recording media for hard disk drives. *J. Appl. Phys.* **102**, 011301, DOI: [10.1063/1.2750414](https://doi.org/10.1063/1.2750414) (2007).
2. Wong, H.-S. P. & Salahuddin, S. Memory leads the way to better computing. *Nat. nanotechnology* **10**, 191–194, DOI: [10.1038/nnano.2015.29](https://doi.org/10.1038/nnano.2015.29) (2015).
3. Linder, J. & Robinson, J. W. Superconducting spintronics. *Nat. Phys.* **11**, 307–315, DOI: [10.1038/nphys3242](https://doi.org/10.1038/nphys3242) (2015).
4. Manchon, A. *et al.* Current-induced spin-orbit torques in ferromagnetic and antiferromagnetic systems. *Rev. Mod. Phys.* **91**, 035004, DOI: [10.1103/RevModPhys.91.035004](https://doi.org/10.1103/RevModPhys.91.035004) (2019).
5. Bass, J. & Pratt, W. P. Spin-diffusion lengths in metals and alloys, and spin-flipping at metal/metal interfaces: an experimentalist's critical review. *J. Condens. Matter Phys.* **19**, 183201, DOI: [10.1088/0953-8984/19/18/183201](https://doi.org/10.1088/0953-8984/19/18/183201) (2007).
6. Birge, N. O. Spin-triplet supercurrents in Josephson junctions containing strong ferromagnetic materials. *Philos. Transactions Royal Soc. A: Math. Phys. Eng. Sci.* **376**, 20150150, DOI: [10.1098/rsta.2015.0150](https://doi.org/10.1098/rsta.2015.0150) (2018).
7. Satchell, N. *et al.* Spin-valve Josephson junctions with perpendicular magnetic anisotropy for cryogenic memory. *Appl. Phys. Lett.* **116**, 022601, DOI: [10.1063/1.5140095](https://doi.org/10.1063/1.5140095) (2020).
8. Satchell, N. *et al.* Pt and CoB trilayer Josephson  $\pi$  junctions with perpendicular magnetic anisotropy. *Sci. Reports* **11**, 11173, DOI: [10.1038/s41598-021-90432-y](https://doi.org/10.1038/s41598-021-90432-y) (2021).
9. Visokay, M. R. & Sinclair, R. Direct formation of ordered CoPt and FePt compound thin films by sputtering. *Appl. Phys. Lett.* **66**, 1692–1694, DOI: [10.1063/1.113895](https://doi.org/10.1063/1.113895) (1995).
10. Iwata, S., Yamashita, S. & Tsunashima, S. Perpendicular magnetic anisotropy and magneto-optical Kerr spectra of MBE-grown PtCo alloy films. *IEEE Transactions on Magn.* **33**, 3670–3672, DOI: [10.1109/20.619533](https://doi.org/10.1109/20.619533) (1997).
11. Cebollada, A. *et al.* Enhanced magneto-optical Kerr effect in spontaneously ordered FePt alloys: Quantitative agreement between theory and experiment. *Phys. Rev. B* **50**, 3419–3422, DOI: [10.1103/PhysRevB.50.3419](https://doi.org/10.1103/PhysRevB.50.3419) (1994).
12. Solovyev, I. V., Dederichs, P. H. & Mertig, I. Origin of orbital magnetization and magnetocrystalline anisotropy in TX ordered alloys (where T=Fe,Co and X=Pt,Pd). *Phys. Rev. B* **52**, 13419–13428, DOI: [10.1103/PhysRevB.52.13419](https://doi.org/10.1103/PhysRevB.52.13419) (1995).
13. Farrow, R. F. C. *et al.* Control of the axis of chemical ordering and magnetic anisotropy in epitaxial FePt films. *J. Appl. Phys.* **79**, 5967–5969, DOI: [10.1063/1.362122](https://doi.org/10.1063/1.362122) (1996).
14. Barmak, K., Ristau, R. A., Coffey, K. R., Parker, M. A. & Howard, J. K. Grain growth and ordering kinetics in CoPt thin films. *J. Appl. Phys.* **79**, 5330–5332, DOI: [10.1063/1.361368](https://doi.org/10.1063/1.361368) (1996).
15. Caro, P. *et al.* The influence of the Pt buffer layer on the perpendicular magnetic anisotropy in epitaxial FePd(001) ordered alloys grown by sputtering. *J. Appl. Phys.* **81**, 5050–5052, DOI: [10.1063/1.364504](https://doi.org/10.1063/1.364504) (1997).
16. Caro, P., Cebollada, A., Briones, F. & Toney, M. Structure and chemical order in sputtered epitaxial FePd (0 0 1) alloys. *J. Cryst. Growth* **187**, 426–434, DOI: [10.1016/S0022-0248\(98\)00036-0](https://doi.org/10.1016/S0022-0248(98)00036-0) (1998).
17. Farrow, R. F. C. *et al.* Magnetic anisotropy and microstructure in molecular beam epitaxial FePt (110)/MgO (110). *J. Appl. Phys.* **84**, 934–939, DOI: [10.1063/1.368158](https://doi.org/10.1063/1.368158) (1998).

18. Thiele, J.-U., Folks, L., Toney, M. F. & Weller, D. K. Perpendicular magnetic anisotropy and magnetic domain structure in sputtered epitaxial FePt (001)  $L_{10}$  films. *J. Appl. Phys.* **84**, 5686–5692, DOI: [10.1063/1.368831](https://doi.org/10.1063/1.368831) (1998).
19. Ristau, R. A., Barmak, K., Lewis, L. H., Coffey, K. R. & Howard, J. K. On the relationship of high coercivity and  $L_{10}$  ordered phase in CoPt and FePt thin films. *J. Appl. Phys.* **86**, 4527–4533, DOI: [10.1063/1.371397](https://doi.org/10.1063/1.371397) (1999).
20. Sun, S., Murray, C. B., Weller, D., Folks, L. & Moser, A. Monodisperse FePt Nanoparticles and Ferromagnetic FePt Nanocrystal Superlattices. *Science* **287**, 1989–1992, DOI: [10.1126/science.287.5460.1989](https://doi.org/10.1126/science.287.5460.1989) (2000).
21. Zeng, H., Yan, M., Powers, N. & Sellmyer, D. J. Orientation-controlled nonepitaxial  $L_{10}$  CoPt and FePt films. *Appl. Phys. Lett.* **80**, 2350–2352, DOI: [10.1063/1.1464663](https://doi.org/10.1063/1.1464663) (2002).
22. Okamoto, S. *et al.* Chemical-order-dependent magnetic anisotropy and exchange stiffness constant of FePt (001) epitaxial films. *Phys. Rev. B* **66**, 024413, DOI: [10.1103/PhysRevB.66.024413](https://doi.org/10.1103/PhysRevB.66.024413) (2002).
23. Chen, J., Xu, Y. & Wang, J. Effect of Pt buffer layer on structural and magnetic properties of FePt thin films. *J. Appl. Phys.* **93**, 1661–1665, DOI: [10.1063/1.1531817](https://doi.org/10.1063/1.1531817) (2003).
24. Zhao, Z., Ding, J., Inaba, K., Chen, J. & Wang, J. Promotion of  $L_{10}$  ordered phase transformation by the Ag top layer on FePt thin films. *Appl. Phys. Lett.* **83**, 2196–2198, DOI: [10.1063/1.1611280](https://doi.org/10.1063/1.1611280) (2003).
25. Sun, S. *et al.* Controlled Synthesis and Assembly of FePt Nanoparticles. *The J. Phys. Chem. B* **107**, 5419–5425, DOI: [10.1021/jp027314o](https://doi.org/10.1021/jp027314o) (2003).
26. Laughlin, D. E., Srinivasan, K., Tanase, M. & Wang, L. Crystallographic aspects of  $L_{10}$  magnetic materials. *Scripta Materialia* **53**, 383–388, DOI: <https://doi.org/10.1016/j.scriptamat.2005.04.039> (2005). Viewpoint set no. 36 on:  $L_{10}$  phases for permanent magnet and recording applications.
27. Barmak, K. *et al.* On the relationship of magnetocrystalline anisotropy and stoichiometry in epitaxial  $L_{10}$  CoPt (001) and FePt (001) thin films. *J. Appl. Phys.* **98**, 033904, DOI: [10.1063/1.1991968](https://doi.org/10.1063/1.1991968) (2005).
28. Liao, W., Chen, S., Yuan, F., Hsu, C. & Lee, H. Thickness dependence of crystallographic and magnetic properties for  $L_{10}$ -CoPt thin films. *J. Magn. Magn. Mater.* **303**, e243–e246, DOI: [10.1016/j.jmmm.2006.01.049](https://doi.org/10.1016/j.jmmm.2006.01.049) (2006). The 6th International Symposium on Physics of Magnetic Materials.
29. Peng, Y., Zhu, J.-G. & Laughlin, D. E.  $L_{10}$  FePt–MgO perpendicular thin film deposited by alternating sputtering at elevated temperature. *J. Appl. Phys.* **99**, 08F907, DOI: [10.1063/1.2176306](https://doi.org/10.1063/1.2176306) (2006).
30. Seemann, K. M. *et al.* Diffusive and ballistic current spin polarization in magnetron-sputtered  $L_{10}$ -ordered epitaxial FePt. *Phys. Rev. B* **76**, 174435, DOI: [10.1103/PhysRevB.76.174435](https://doi.org/10.1103/PhysRevB.76.174435) (2007).
31. Li, X. H. *et al.* Atomic ordering kinetics of FePt thin films: Nucleation and growth of  $L_{10}$  ordered domains. *J. Appl. Phys.* **101**, 093911, DOI: [10.1063/1.2730568](https://doi.org/10.1063/1.2730568) (2007).
32. Sato, H. *et al.* Fabrication of  $L_{11}$  type Co-Pt ordered alloy films by sputter deposition. *J. Appl. Phys.* **103**, 07E114, DOI: [10.1063/1.2830097](https://doi.org/10.1063/1.2830097) (2008).
33. Chen, J., Sun, C., Chow, G. M. *et al.* A review of  $L_{10}$  FePt films for high-density magnetic recording. *Int. J. Prod. Dev.* **5**, 238 (2008).
34. Varvaro, G. *et al.* Study of Magnetic Easy Axis 3-D Arrangement in  $L_{10}$  CoPt(111)/Pt(111)/MgO(100) Tilted System for Perpendicular Recording. *IEEE Transactions on Magn.* **44**, 643–647, DOI: [10.1109/TMAG.2008.918205](https://doi.org/10.1109/TMAG.2008.918205) (2008).
35. Hsiao, S. N. *et al.* Effect of initial stress/strain state on order-disorder transformation of FePt thin films. *Appl. Phys. Lett.* **94**, 232505, DOI: [10.1063/1.3153513](https://doi.org/10.1063/1.3153513) (2009).
36. Seemann, K. M., Hickey, M. C., Baltz, V., Hickey, B. J. & Marrows, C. H. Spin-dependent scattering and the spin polarization of a diffusive current in partly disordered  $L_{10}$  epitaxial FePd. *New J. Phys.* **12**, 033033, DOI: [10.1088/1367-2630/12/3/033033](https://doi.org/10.1088/1367-2630/12/3/033033) (2010).
37. Yuan, F.-T., Sun, A.-C. & Hsu, J.-H. Effect of underlayer (Pt, Ru, Au, Ag) on  $L_{11}$  ordering in sputtered CoPt thin films. *Scr. Mater.* **62**, 762–765, DOI: [10.1016/j.scriptamat.2010.02.008](https://doi.org/10.1016/j.scriptamat.2010.02.008) (2010).
38. Dannenberg, A., Gruner, M. E. & Entel, P. First-principles study of the structural stability of  $L_{11}$  order in Pt-based alloys. *J. Physics: Conf. Ser.* **200**, 072021, DOI: [10.1088/1742-6596/200/7/072021](https://doi.org/10.1088/1742-6596/200/7/072021) (2010).
39. Yang, Y., Chen, J. S. & Chow, G. M. Highly chemical ordered  $L_{11}$  CoPt (111) films with perpendicular anisotropy grown on glass substrates. *J. Appl. Phys.* **109**, 07B744, DOI: [10.1063/1.3561115](https://doi.org/10.1063/1.3561115) (2011).

40. Ohtake, M., Ouchi, S., Kirino, F. & Futamoto, M. L10 ordered phase formation in FePt, FePd, CoPt, and CoPd alloy thin films epitaxially grown on MgO(001) single-crystal substrates. *J. Appl. Phys.* **111**, 07A708, DOI: [10.1063/1.3672856](https://doi.org/10.1063/1.3672856) (2012).
41. Ohtake, M., Ouchi, S., Kirino, F. & Futamoto, M. Structure and magnetic properties of CoPt, CoPd, FePt, and FePd alloy thin films formed on MgO (111) substrates. *IEEE Trans. Magn.* **48**, 3595–3598, DOI: [10.1109/TMAG.2012.2198875](https://doi.org/10.1109/TMAG.2012.2198875) (2012).
42. Sun, A.-C., Huang, S. & Huang, C.-F. Formation of rhombohedral L1<sub>1</sub> CoPt thin film on glass and MgO (111) substrate. *J. Magn. Magn. Mater.* **345**, 282–287, DOI: [10.1016/j.jmmm.2013.07.003](https://doi.org/10.1016/j.jmmm.2013.07.003) (2013).
43. Sun, A.-C. & Huang, C.-F. Microstructure study of CoPt thin film with phase change from A1 → L1<sub>1</sub> → A1 → L1<sub>0</sub>. *J. Appl. Phys.* **113**, DOI: [10.1063/1.4799526](https://doi.org/10.1063/1.4799526) (2013).
44. Varaprasad, B. S. D. C. S., Chen, M., Takahashi, Y. K. & Hono, K. L1<sub>0</sub>-Ordered FePt-Based Perpendicular Magnetic Recording Media for Heat-Assisted Magnetic Recording. *IEEE Transactions on Magn.* **49**, 718–722, DOI: [10.1109/TMAG.2012.2218227](https://doi.org/10.1109/TMAG.2012.2218227) (2013).
45. Ohtake, M., Suzuki, D., Kirino, F. & Futamoto, M. Structure analysis of CoPt alloy film with metastable ordered phases of L1<sub>1</sub> and Bh formed on Ru (0001) underlayer. In *EPJ Web of Conferences*, vol. 75, 06003, DOI: [10.1051/epjconf/20147506003](https://doi.org/10.1051/epjconf/20147506003) (EDP Sciences, 2014).
46. Varvaro, G., Laureti, S. & Fiorani, D. L10 FePt-based thin films for future perpendicular magnetic recording media. *J. Magn. Magn. Mater.* **368**, 415–420, DOI: <https://doi.org/10.1016/j.jmmm.2014.04.058> (2014).
47. Futamoto, M., Nakamura, M., Ohtake, M., Inaba, N. & Shimotsu, T. Growth of L10-ordered crystal in FePt and FePd thin films on MgO(001) substrate. *AIP Adv.* **6**, 085302, DOI: [10.1063/1.4960554](https://doi.org/10.1063/1.4960554) (2016).
48. Zygridou, S., Barton, C., Nutter, P. & Thomson, T. Exploring the potential of remote plasma sputtering for the production of L10 ordered FePt thin films. *J. Phys. D: Appl. Phys.* **50**, 275005, DOI: [10.1088/1361-6463/aa761a](https://doi.org/10.1088/1361-6463/aa761a) (2017).
49. Griffiths, R. A. *et al.* Temperature-Dependent Studies of Coupled Fe<sub>55</sub>Pt<sub>45</sub>/Fe<sub>49</sub>Rh<sub>51</sub> Thin Films. *Phys. Rev. Appl.* **10**, 054015, DOI: [10.1103/PhysRevApplied.10.054015](https://doi.org/10.1103/PhysRevApplied.10.054015) (2018).
50. Gao, Y. *et al.* Formation mechanism of rhombohedral L11 phase in CoPt films grown on glass substrate. *J. Magn. Magn. Mater.* **471**, 406–410, DOI: [10.1016/j.jmmm.2018.09.120](https://doi.org/10.1016/j.jmmm.2018.09.120) (2019).
51. Chiou, J.-Y., Chang, H. W., Chi, C.-C., Hsiao, C.-H. & Ouyang, C. L10 FePt Films with Optimal (001) Texture on Amorphous SiO<sub>2</sub>/Si Substrates for High-Density Perpendicular Magnetic Recording Media. *ACS Appl. Nano Mater.* **2**, 5663–5673, DOI: [10.1021/acsanm.9b01192](https://doi.org/10.1021/acsanm.9b01192) (2019).
52. Griggs, W. *et al.* Polarized neutron reflectometry characterization of interfacial magnetism in an FePt/FeRh exchange spring. *Phys. Rev. Mater.* **6**, 024403, DOI: [10.1103/PhysRevMaterials.6.024403](https://doi.org/10.1103/PhysRevMaterials.6.024403) (2022).
53. Spencer, B. *et al.* Characterization of buried interfaces using Ga K $\alpha$  hard X-ray photoelectron spectroscopy (HAXPES). *Faraday Discuss.* DOI: [10.1039/D2FD00021K](https://doi.org/10.1039/D2FD00021K) (2022).
54. Liu, L. *et al.* Electrical switching of perpendicular magnetization in a single ferromagnetic layer. *Phys. Rev. B* **101**, 220402, DOI: [10.1103/PhysRevB.101.220402](https://doi.org/10.1103/PhysRevB.101.220402) (2020).
55. Zhu, L., Zhang, X. S., Muller, D. A., Ralph, D. C. & Buhrman, R. A. Observation of strong bulk damping-like spin-orbit torque in chemically disordered ferromagnetic single layers. *Adv. Funct. Mater.* **30**, 2005201, DOI: [10.1002/adfm.202005201](https://doi.org/10.1002/adfm.202005201) (2020).
56. Zheng, S. Q. *et al.* Disorder dependent spin–orbit torques in L1<sub>0</sub> FePt single layer. *Appl. Phys. Lett.* **117**, 242403, DOI: [10.1063/5.0028815](https://doi.org/10.1063/5.0028815) (2020).
57. Liu, L. *et al.* Symmetry-dependent field-free switching of perpendicular magnetization. *Nat. Nanotechnol.* **16**, 277–282, DOI: [10.1038/s41565-020-00826-8](https://doi.org/10.1038/s41565-020-00826-8) (2021).
58. Tao, Y. *et al.* Magnetization switching by spin–orbit torque in L1<sub>0</sub>-FePt and Ta/FePt films with large perpendicular magnetic anisotropy. *IEEE Transactions on Magn.* **58**, 1–4, DOI: [10.1109/TMAG.2021.3081510](https://doi.org/10.1109/TMAG.2021.3081510) (2022).
59. Dong, K. *et al.* Current-induced magnetic switching in an L1<sub>0</sub> FePt single layer with large perpendicular anisotropy through spin–orbit torque. *Engineering* DOI: [10.1016/j.eng.2021.09.018](https://doi.org/10.1016/j.eng.2021.09.018) (2022).
60. Tao, Y. *et al.* Field-free spin–orbit torque switching in L1<sub>0</sub>-FePt single layer with tilted anisotropy. *Appl. Phys. Lett.* **120**, 102405, DOI: [10.1063/5.0077465](https://doi.org/10.1063/5.0077465) (2022).



61. Liu, L. *et al.* Current-induced self-switching of perpendicular magnetization in CoPt single layer. *Nat. Commun.* **13**, 1–8, DOI: [10.1038/s41467-022-31167-w](https://doi.org/10.1038/s41467-022-31167-w) (2022).
62. Wildes, A., Mayer, J. & Theis-Bröhl, K. The growth and structure of epitaxial niobium on sapphire. *Thin Solid Films* **401**, 7–34, DOI: [10.1016/S0040-6090\(01\)01631-5](https://doi.org/10.1016/S0040-6090(01)01631-5) (2001).
63. Satchell, N. & Birge, N. O. Supercurrent in ferromagnetic Josephson junctions with heavy metal interlayers. *Phys. Rev. B* **97**, 214509, DOI: [10.1103/PhysRevB.97.214509](https://doi.org/10.1103/PhysRevB.97.214509) (2018).
64. Mihai, A. P. *et al.* Effect of substrate temperature on the magnetic properties of epitaxial sputter-grown Co/Pt. *Appl. Phys. Lett.* **103**, 262401, DOI: [10.1063/1.4856395](https://doi.org/10.1063/1.4856395) (2013).
65. McCurrie, R. & Gaunt, P. The magnetic anisotropy of ordered equiatomic platinum cobalt. *Philos. Mag.* **19**, 339–347, DOI: [10.1080/14786436908217790](https://doi.org/10.1080/14786436908217790) (1969).
66. Björck, M. & Andersson, G. GenX: an extensible X-ray reflectivity refinement program utilizing differential evolution. *J. Appl. Crystallogr.* **40**, 1174–1178, DOI: [10.1107/S0021889807045086](https://doi.org/10.1107/S0021889807045086) (2007).
67. Moon, K.-W., Lee, J.-C., Choe, S.-B. & Shin, K.-H. Determination of perpendicular magnetic anisotropy in ultrathin ferromagnetic films by extraordinary Hall voltage measurement. *Rev. Sci. Instrum.* **80**, 113904, DOI: [10.1063/1.3262635](https://doi.org/10.1063/1.3262635) (2009).
68. Schütz, G. *et al.* Spin-dependent x-ray absorption in Co/Pt multilayers and Co<sub>50</sub>Pt<sub>50</sub> alloy. *J. Appl. Phys.* **67**, 4456–4458, DOI: [10.1063/1.344903](https://doi.org/10.1063/1.344903) (1990).
69. Geissler, J. *et al.* Pt magnetization profile in a Pt/Co bilayer studied by resonant magnetic x-ray reflectometry. *Phys. Rev. B* **65**, 020405(R), DOI: [10.1103/PhysRevB.65.020405](https://doi.org/10.1103/PhysRevB.65.020405) (2001).
70. Suzuki, M. *et al.* Depth profile of spin and orbital magnetic moments in a subnanometer Pt film on Co. *Phys. Rev. B* **72**, 054430, DOI: [10.1103/PhysRevB.72.054430](https://doi.org/10.1103/PhysRevB.72.054430) (2005).
71. Rowan-Robinson, R. M. *et al.* The interfacial nature of proximity-induced magnetism and the Dzyaloshinskii-Moriya interaction at the Pt/Co interface. *Sci. Rep.* **7**, 16835, DOI: [10.1038/s41598-017-17137-z](https://doi.org/10.1038/s41598-017-17137-z) (2017).
72. Inyang, O. *et al.* Threshold interface magnetization required to induce magnetic proximity effect. *Phys. Rev. B* **100**, 174418, DOI: [10.1103/PhysRevB.100.174418](https://doi.org/10.1103/PhysRevB.100.174418) (2019).
73. Soulen, R. J. *et al.* Measuring the Spin Polarization of a Metal with a Superconducting Point Contact. *Science* **282**, 85–88, DOI: [10.1126/science.282.5386.85](https://doi.org/10.1126/science.282.5386.85) (1998).
74. Baltz, V. *et al.* Conductance features in point contact Andreev reflection spectra. *J. Physics: Condens. Matter* **21**, 095701, DOI: [10.1088/0953-8984/21/9/095701](https://doi.org/10.1088/0953-8984/21/9/095701) (2009).
75. Naylor, A. D., Burnell, G. & Hickey, B. J. Transport spin polarization of the rare-earth transition-metal alloy Co<sub>1-x</sub>Gd<sub>x</sub>. *Phys. Rev. B* **85**, 064410, DOI: [10.1103/PhysRevB.85.064410](https://doi.org/10.1103/PhysRevB.85.064410) (2012).
76. Ma’Mari, F. A. *et al.* Direct Measurement of Spin Polarization in Ferromagnetic-C60 Interfaces Using Point-Contact Andreev Reflection. *IEEE Transactions on Magn.* **50**, 1–4, DOI: [10.1109/TMAG.2014.2322658](https://doi.org/10.1109/TMAG.2014.2322658) (2014).
77. Strijkers, G. J., Ji, Y., Yang, F. Y., Chien, C. L. & Byers, J. M. Andreev reflections at metal/superconductor point contacts: Measurement and analysis. *Phys. Rev. B* **63**, 104510, DOI: [10.1103/PhysRevB.63.104510](https://doi.org/10.1103/PhysRevB.63.104510) (2001).
78. Yates, K. A. & Cohen, L. F. Andreev reflection spectroscopy in transition metal oxides. *Philos. Trans. R. Soc. A Math. Phys. Eng. Sci.* **376**, 20150001, DOI: [10.1098/rsta.2015.0001](https://doi.org/10.1098/rsta.2015.0001) (2018).
79. The Royce Deposition System is a multi-chamber, multi-technique thin film deposition tool based at the University of Leeds as part of the [Henry Royce Institute](https://www.henryroyceinstitute.co.uk/).

## Acknowledgements

We wish to thank R. Hunt, M. Ali and M. C. Rosamond for experimental assistance. We acknowledge support from the Henry Royce Institute. The work was supported financially through the following EPSRC grants: EP/V028138/1.

## Author Contributions Statement

N.S. and G.B. conceived and designed the study. N.S. with S.G., M.M., M.R., O.C. and G.B. undertook the measurements and analysed the data. N.S. and P.M.S. undertook the materials development. N.S. undertook the sample growth and fabrication. N.S. with G.B. wrote the manuscript. All authors reviewed and edited the manuscript.

## **Additional Information**

**Supplementary information** accompanies this paper at URL.

**Competing interests:** The authors declare no competing interests.

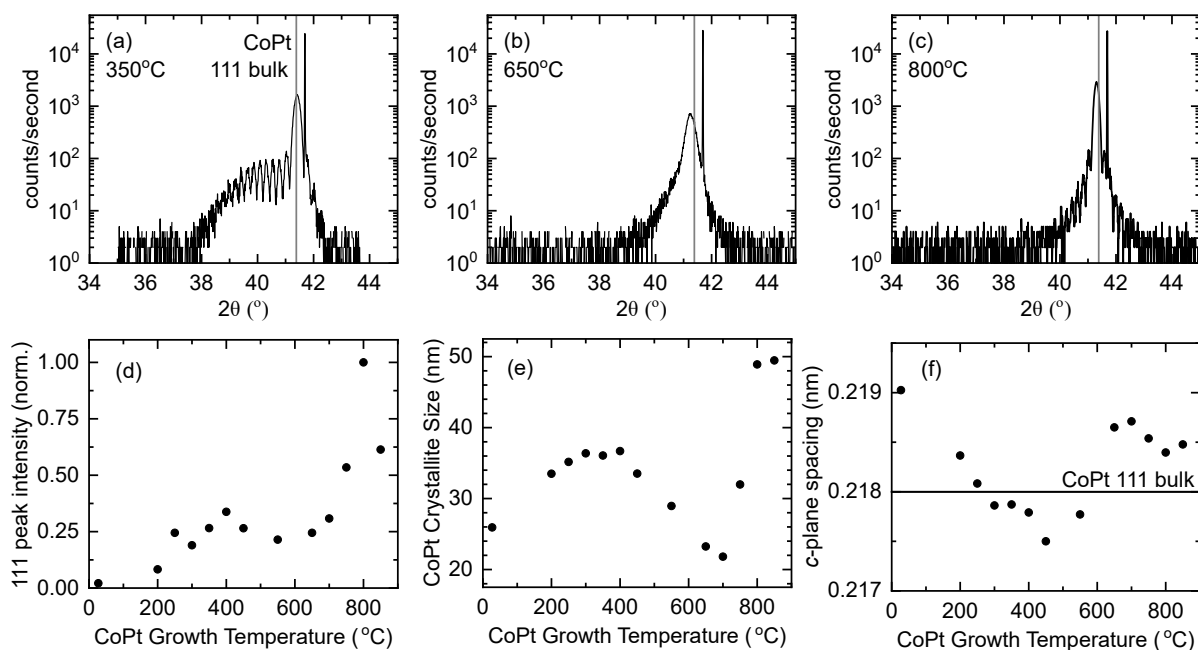


**Figure 1.** Structural characterisation of Al<sub>2</sub>O<sub>3</sub>(sub)/Pt(4 nm)/CoPt(40 nm)/Pt(4 nm) sheet films grown at different set temperatures obtained by x-ray diffraction measurements. (a-c) X-ray diffraction data for samples at selected growth temperatures. The position of the main [111] structural peak for the CoPt layer is indicated. (d) The normalised CoPt [111] peak intensity. (e) The CoPt crystallite size determined from the CoPt [111] peak Gaussian full width half maximum value. (f) The CoPt *c*-plane spacing. Uncertainties in the peak intensity, crystallite size, and *c*-plane spacing are smaller than the data symbols.

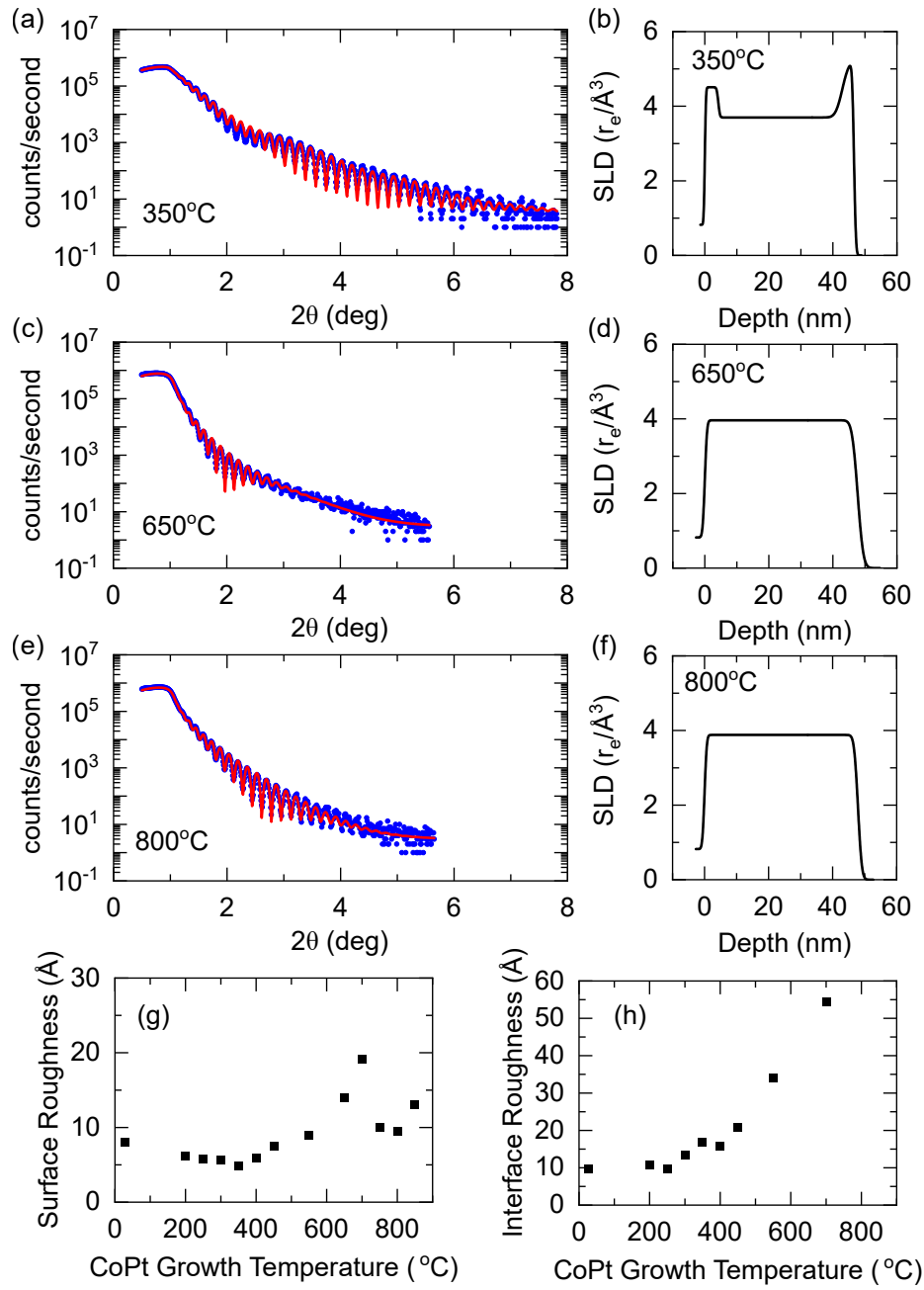


**Figure 2.** Structural characterisation of  $\text{Al}_2\text{O}_3(\text{sub})/\text{Pt}(4\text{ nm})/\text{CoPt}(40\text{ nm})/\text{Pt}(4\text{ nm})$  sheet films grown at different set temperatures obtained by x-ray reflectivity measurements. (a,c,e) X-ray reflectivity data for samples at selected growth temperatures. The reflectivity is fit to a best fit model, which is shown correspondingly in (b,d,f). (g) The surface roughness parameter extracted from the best fit model. (h) The interfacial roughness parameter from the model, indicating the interdiffusion between the CoPt and Pt layers.



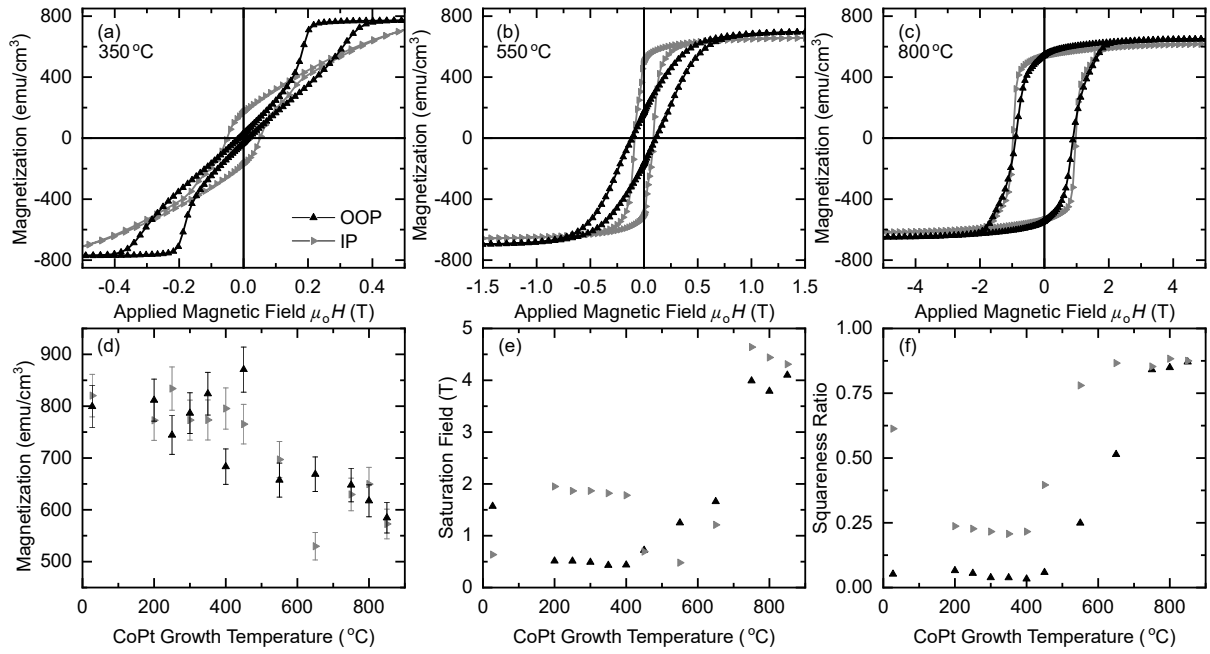


**Figure 3.** Magnetisation characterisation of Al<sub>2</sub>O<sub>3</sub>(sub)/Pt(4 nm)/CoPt(40 nm)/Pt(4 nm) sheet films grown at different set temperatures with the applied field oriented out-of-plane ( $\blacktriangle$ ) and in-plane ( $\blacktriangleright$ ). (a-c) Magnetic hysteresis loops acquired at a temperature of 300 K. The sample growth temperature is (a) 350°C, corresponding to  $L1_1$  crystal structure, (b) 550°C, corresponding to disordered  $A_1$  growth, and (c) 800°C, corresponding to  $L1_0$  crystal structure. The diamagnetic contribution from the substrate has been subtracted. (d-f) Trends in the magnetic characterisation as a function of sample growth temperature, (d) magnetisation, (e) saturation field and (f) squareness ratio ( $M_r/M_s$ ). Magnetisation is calculated from the measured total magnetic moments, the areas of the sample portions, and the nominal thickness of the CoPt layer (40 nm). The significant contribution to the uncertainty in magnetisation is from the area measurements of the sample portions.

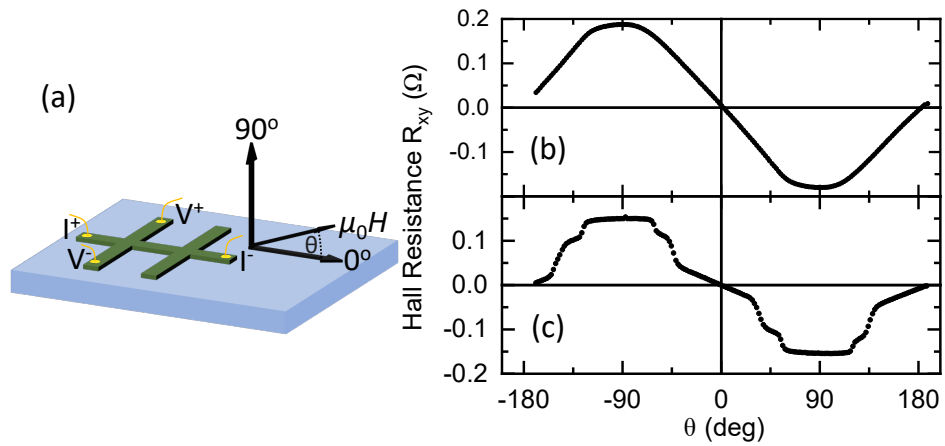


**Figure 4.** In-plane to out-of-plane angular dependent Hall resistance for  $\text{Al}_2\text{O}_3(\text{sub})/\text{Pt}(4\text{ nm})/\text{CoPt}(40\text{ nm})/\text{Pt}(4\text{ nm})$ . (a) Schematic of Hall bar devices, measurement geometry, and applied field direction. Hall resistance versus angle for (b) the  $L1_1$  crystal structure ( $350^\circ\text{C}$  growth temperature) at 0.4 T and (c)  $L1_0$  crystal structure ( $800^\circ\text{C}$ ) at 3 T. Data acquired at a temperature of 295 K.

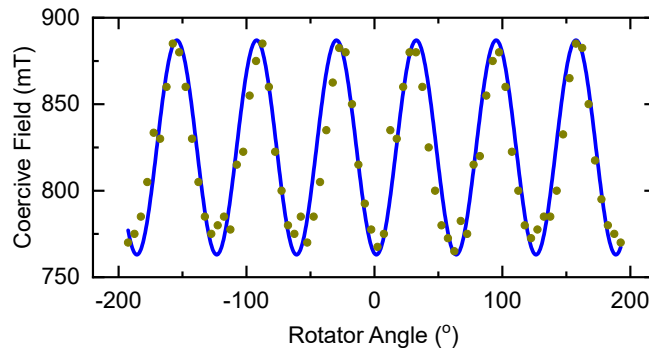


**Figure 5.** In-plane rotation of the  $\text{Al}_2\text{O}_3(\text{sub})/\text{Pt}(4\text{ nm})/\text{CoPt}(128\text{ nm})/\text{Pt}(4\text{ nm})$  sample with  $L1_0$  crystal structure ( $800^\circ\text{C}$ ). The coercive field is extracted from the hysteresis loop measured at each rotator angle. The position of  $0^\circ$  is arbitrary. The line shows a best fit sine function as a guide for the eye. Data acquired at a temperature of 300 K.

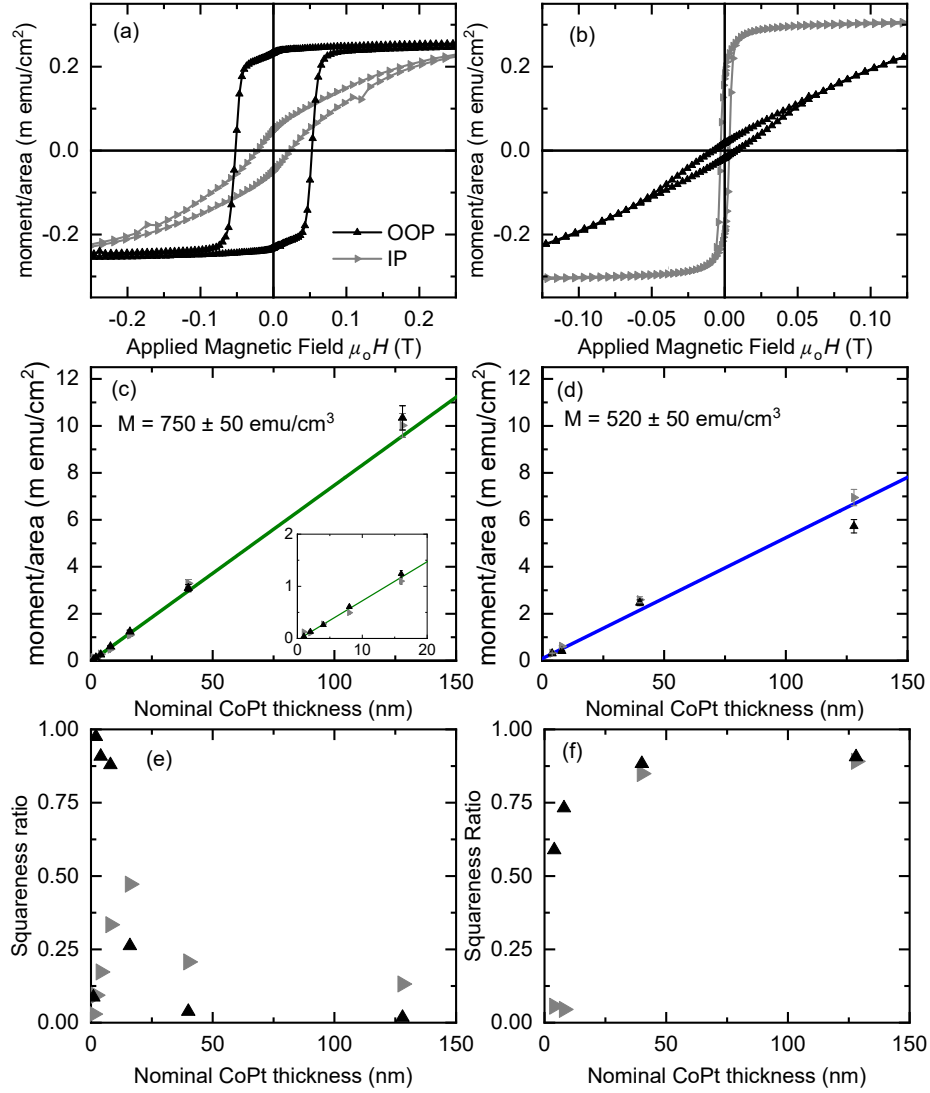


**Figure 6.** Magnetisation characterisation of  $\text{Al}_2\text{O}_3(\text{sub})/\text{Pt}(4 \text{ nm})/\text{CoPt}(d_{\text{CoPt}})/\text{Pt}(4 \text{ nm})$  sheet films with the applied field oriented out-of-plane ( $\blacktriangle$ ) and in-plane ( $\blacktriangleright$ ). (a,b) Magnetic hysteresis loops acquired at a temperature of 300 K for  $d_{\text{CoPt}} = 4 \text{ nm}$ . The sample growth temperature is (a) 350°C, corresponding to  $L_{11}$  crystal structure, (b) 800°C, corresponding to  $L_{10}$  crystal structure. The diamagnetic contribution from the substrate has been subtracted. (c,d) Magnetic moment per area versus  $d_{\text{CoPt}}$  for growth temperature of (c) 350°C (with zoomed region inset) and (d) 800°C. The significant contribution to the uncertainty in moment/area is from the area measurements of the sample portions. The magnetisation and uncertainty therein is determined from the fit to Eqn. 1 (solid lines) and gives a best fit of  $M = 750 \pm 50 \text{ emu/cm}^3$  and  $M = 520 \pm 50 \text{ emu/cm}^3$  for the  $L_{11}$  and  $L_{10}$  crystal structures respectively. (e,f) The squareness ratio ( $M_s/M_r$ ) versus  $d_{\text{CoPt}}$  for growth temperature of (e) 350°C and (f) 800°C.



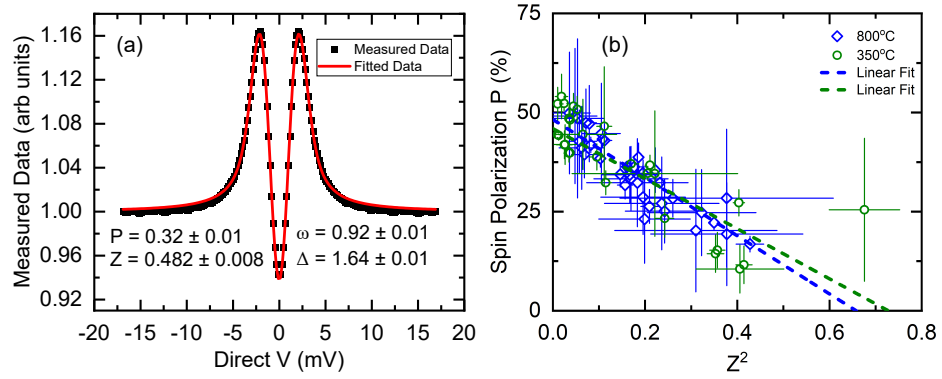


**Figure 7.** Point contact Andreev reflection measurements on the  $\text{Al}_2\text{O}_3(\text{sub})/\text{Pt}(4\text{ nm})/\text{CoPt}(128\text{ nm})/\text{Pt}(4\text{ nm})$  samples grown at  $350^\circ\text{C}$ , corresponding to  $L_{11}$  crystal structure, and  $800^\circ\text{C}$ , corresponding to  $L_{10}$  crystal structure. (a) Exemplar conductance versus voltage curve for the  $L_{10}$  sample with best fit to the BKT model (see text). (b) The polarisation is shown as a function of the square of the barrier strength,  $Z^2$ , with linear fits to the data.

# Supplementary Information for “Thin film epitaxial [111] Co<sub>50</sub>Pt<sub>50</sub>: Structure, magnetisation, and spin polarisation”

N. Satchell<sup>1</sup>, S. Gupta<sup>1</sup>, M. Maheshwari<sup>1</sup>, P. M. Shepley<sup>1</sup>, M. Rogers<sup>1</sup>, O. Cespedes<sup>1</sup>, and G. Burnell<sup>1,\*</sup>

<sup>1</sup>School of Physics and Astronomy, University of Leeds, Leeds, LS2 9JT, United Kingdom

\*g.burnell@leeds.ac.uk

## ABSTRACT

This Supplementary Information contains additional analysis and data in support of the conclusions presented in the main text.

## X-ray Diffraction Data

Figures S1, S2, S3 show a complete set of X-ray diffraction scans for samples grown at each temperature. The very sharp peak at  $2\theta \approx 42^\circ$  is from the c-plane sapphire (0006) plane with  $\{111\}$  peaks from the CoPt phase clearly visible to left. The substrate (00012) and CoPt  $\{222\}$  peaks are also present close to  $2\theta$  of  $90^\circ$ . Samples grown at  $200 - 450^\circ\text{C}$  and also at  $800^\circ\text{C}$  clearly exhibit Pendellosung fringes, indicative of good crystal ordering from the  $L1_1$  and  $L1_0$  phases. The peak intensity and FWHM shown in the main text are extracted from a Gaussian peak fit to the CoPt  $\{111\}$  peak data, although similar data could be obtained from the CoPt  $\{222\}$  data. Figure S4 shows the XRD on the 40 nm and 128 nm samples grown at  $350^\circ\text{C}$ . The additional peak at  $\approx 21^\circ$  in the 128 nm sample we interpret as the superstructure peak from the  $L1_1$  growth.

## X-ray Reflectivity Data

Growth Temp (°C)	Al <sub>2</sub> O <sub>3</sub> $\sigma$ (Å)	Pt1 $d$ (Å)	$\sigma$ (Å)	$\rho$ (f.u./Å <sup>3</sup> )	CoPt $d$ (Å)	$\sigma$ (Å)	$\rho$ (f.u./Å <sup>3</sup> )	Pt2 $d$ (Å)	$\sigma$ (Å)	$\rho$ (f.u./Å <sup>3</sup> )
27	4.9	42.8	5.6	0.0615	385	9.6	0.0758	40.9	8.0	0.0713
200	3.7	44.8	3.3	0.0615	382	10.8	0.0758	39.0	6.2	0.0713
250	3.3	46.0	3.9	0.0615	381	9.7	0.0758	40.8	5.8	0.0713
300	3.2	43.2	3.8	0.0615	388	13.5	0.0758	37.2	5.7	0.0713
350	2.8	42.1	4.1	0.0615	387	16.9	0.0758	36.4	4.8	0.0713
400	2.6	41.5	4.6	0.0615	388	15.7	0.0758	39.4	5.9	0.0713
450	3.3	41.1	4.1	0.0615	395	20.7	0.0758	32.2	7.5	0.0713
550	4.6				445	34.0	0.0758	29.6	8.9	0.0641
650	5.0				477	14.0	0.0812			
700	5.4	7.6	4.2	0.0615	385	54.5	0.0758	61.6	19.1	0.0564
750	4.4				481	10.0	0.0786			
800	5.4				479	9.5	0.0796			
850	5.2				493	13.0	0.0724			

Figures S5, S6, S7 show a complete set of X-ray reflectivity scans for samples grown at each temperature. The data with best fits are shown on the left, with the model corresponding to the best fit on the right side. The XRR are fit using the GenX package<sup>1</sup>. The extracted fitting parameters are given in the following table. Each layer is modelled as a box with a thickness ( $d$ ) and a roughness ( $\sigma$ ), in units of Å, and a density ( $\rho$ ), in units of formula unit (f.u.)/Å<sup>3</sup>. The substrate has only a roughness fitting parameter as the model treats it as an infinitely thick box with the bulk density of Al<sub>2</sub>O<sub>3</sub>. “Pt1” layer is the seed layer and “Pt2” is the capping layer. Between  $27^\circ\text{C}$  and  $450^\circ\text{C}$ , the best fit model is for the as-intended trilayer. Between these temperatures the density is fixed and only the thickness and roughness are free fit parameters. The slight difference in density

between the seed and capping layer indicates that the top surface of “Pt2” is oxidized. At higher temperatures the trilayer model breaks down and alternative fitting to either a single, bi-, or tri-layer model is used.

## Magnetometry

Magnetic hysteresis loops were measured for a set of samples of common thickness grown at temperatures from room temperature to 850° C with the field applied in the plane of the substrate and perpendicular to the substrate plane - shown in Figure S8. For the data shown here, a diamagnetic background resulting from the substrate and sample stick has been removed. The saturation magnetisation is determined by fitting a line to the outer section of the upper and lower branches and taking the difference in intercepts with the  $H = 0$  axis. The uncertainty is dominated by the determination of the sample area. The saturation field is determined from the point at which the measured data has deviated from the saturation magnetisation by more than twice the scatter in the data in the saturated regions of the loop. Figures S9 and S10 show similar magnetic hysteresis loops for samples of increasing thickness grown at 350° C and 800° C respectively.

## PCAR

The Point Contact Andreev Reflection spectra are measured by an AC lockin technique where the contact is subjected to a controlled DC bias with a small AC modulation which is sensed across the contact and across a control resistor to allow a differential conductance to be determined. The DC bias is separately monitored as it is adjusted to give a tip bias typically in the range of  $\approx \pm 30$  meV. The DC bias is swept over 6 quarters from 0 to maximum and then to minimum and back to maximum and finally to zero. We only analyse the parts of the trace from maximum to minimum and back to maximum. The measured DC bias is subject to a small instrumentation offset which is removed at this first stage of data processing. Since all the features of interest in the spectra should be symmetrical about zero bias, we decompose the data into symmetric and anti-symmetric parts and retain only the symmetric part. The BTK model is usually considered in terms of the normalised conductance of the contact – normalised to the conductance at high bias where transfer between electron/hole states in the ferromagnetic and electron/hole-like quasiparticles in the superconductor. In this high bias regime it is possible in some contact to get parabolic conductance due to tunnelling or Joule heating effects<sup>2</sup> and so we normalise the experimental data by dividing through a parabola fitted to the outer 20% of the spectra.

The modified BTK model used in the analysis of the PCAR data has 4 fitting parameters. Firstly, an interfacial barrier strength  $Z$  that is dimensionless. This effectively determines a scattering potential at the interface and so even in a perfect contact will take a small, but finite, value. Secondly, the spin polarisation  $P = \frac{N_{\uparrow}v_{f\uparrow} - N_{\downarrow}v_{f\downarrow}}{N_{\uparrow}v_{f\uparrow} + N_{\downarrow}v_{f\downarrow}}$  which thus ranges from 0 for non-spin-polarised materials to 1 for fully spin-polarised materials. Thirdly, the superconducting energy gap  $\Delta$  which might reasonably be expected not to be fully bulk like at the tip of the contact. Finally there is a ‘smearing parameter’  $\omega$  that encompasses both thermal effects and athermal scattering processes not otherwise accounted for in the model.

The modified BTK model is then fitted to the now normalised data. We start with an initial set of fitting values of  $Z = 0.5$ ,  $\omega = 0.5$  meV (c.f.  $4.2\text{ K} \equiv 0.36\text{ meV}$ ),  $\Delta = 1.5$  meV and  $P = 0.5$ . We use a differential-evolution algorithm to identify a global minimum  $\chi^2$  value to locate the best fit. This best-fit location is then used to seed a non-linear least squares fit using the Levenberg–Marquardt algorithm, allowing us to determine estimated standard errors for the fitting parameters.

We then discard fits with non-physical values of  $\Delta$ , excessively large  $\omega$  – both of which would indicate an unaccounted spreading resistance, before considering all the fitted  $(Z, P)$  combinations. As noted in the main text, the extrapolation back to  $Z^2 = 0$  is not strictly physical, however, in practice in an all-metal system, very low values of  $Z$  with uncertainties that encompass  $Z = 0$  can be obtained.

## References

1. Björck, M. & Andersson, G. *GenX*: an extensible X-ray reflectivity refinement program utilizing differential evolution. *J. Appl. Crystallogr.* **40**, 1174–1178, DOI: [10.1107/S0021889807045086](https://doi.org/10.1107/S0021889807045086) (2007).
2. Baltz, V. *et al.* Conductance features in point contact Andreev reflection spectra. *J. Physics: Condens. Matter* **21**, 095701, DOI: [10.1088/0953-8984/21/9/095701](https://doi.org/10.1088/0953-8984/21/9/095701) (2009).

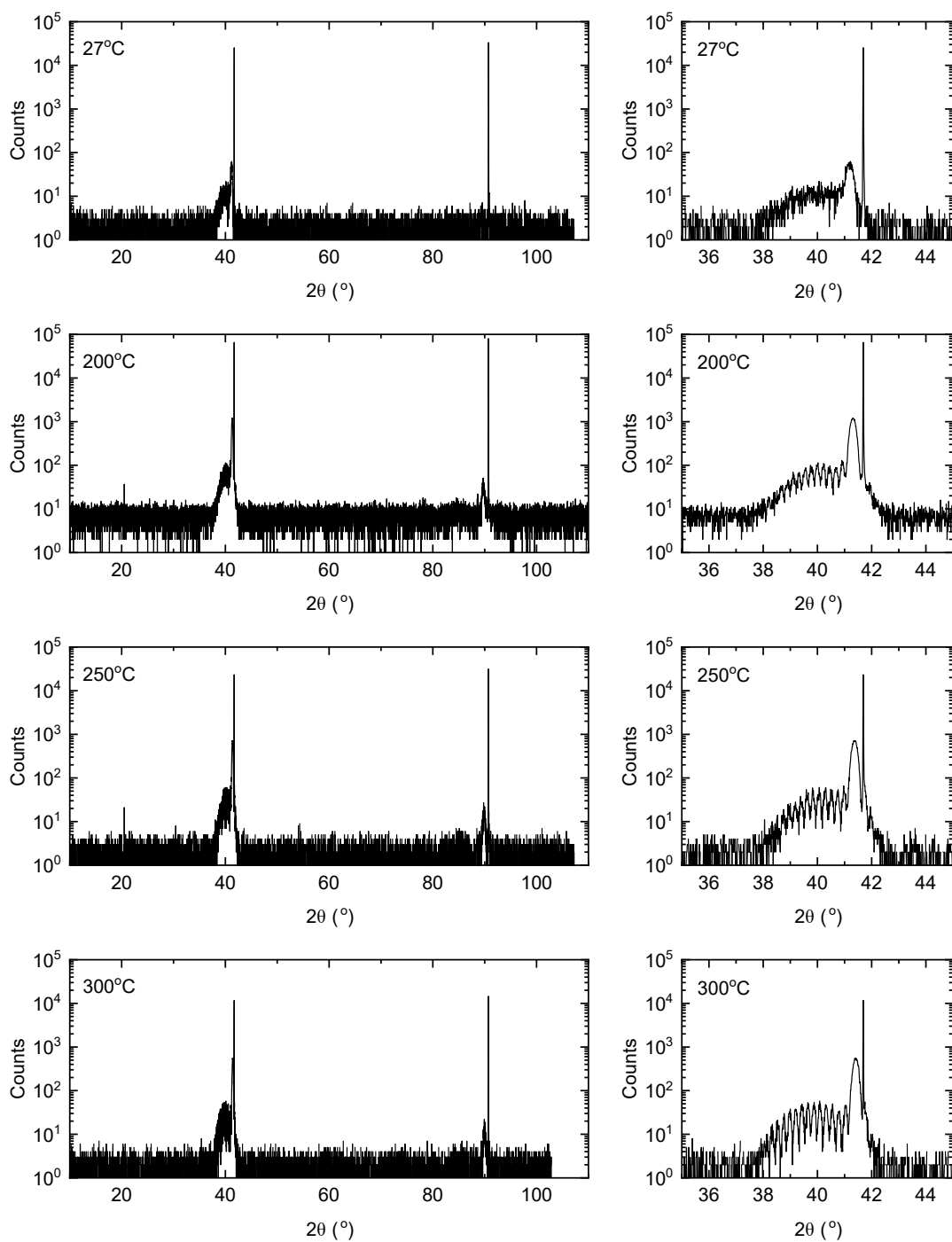


**Figure S1.** X-ray diffraction for the growth temperature set of samples reported in the main text. Left column: Full data range. Right column: Cropped region around the 111 structural peak.



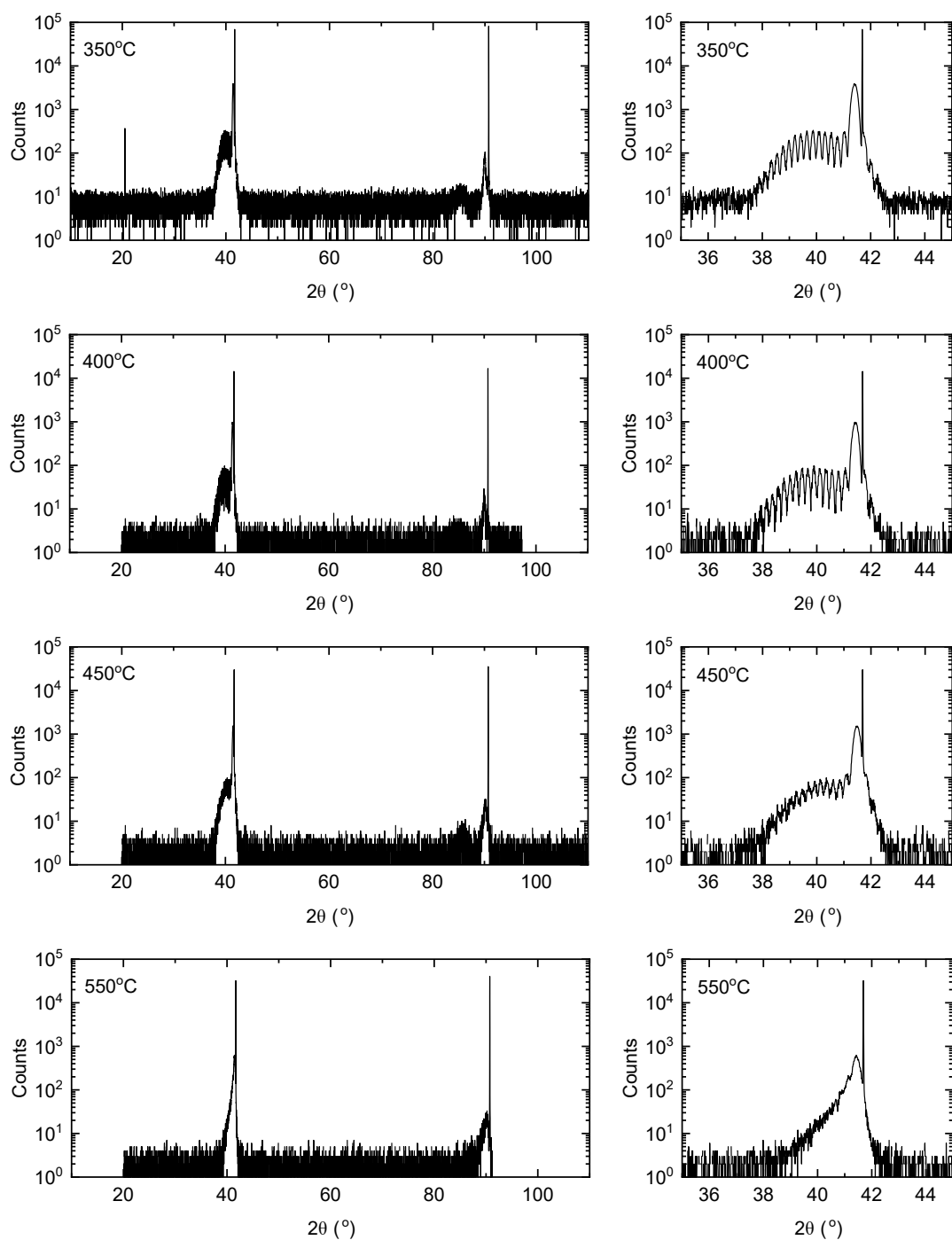


**Figure S2.** X-ray diffraction for the growth temperature set of samples reported in the main text. Left column: Full data range. Right column: Cropped region around the 111 structural peak.

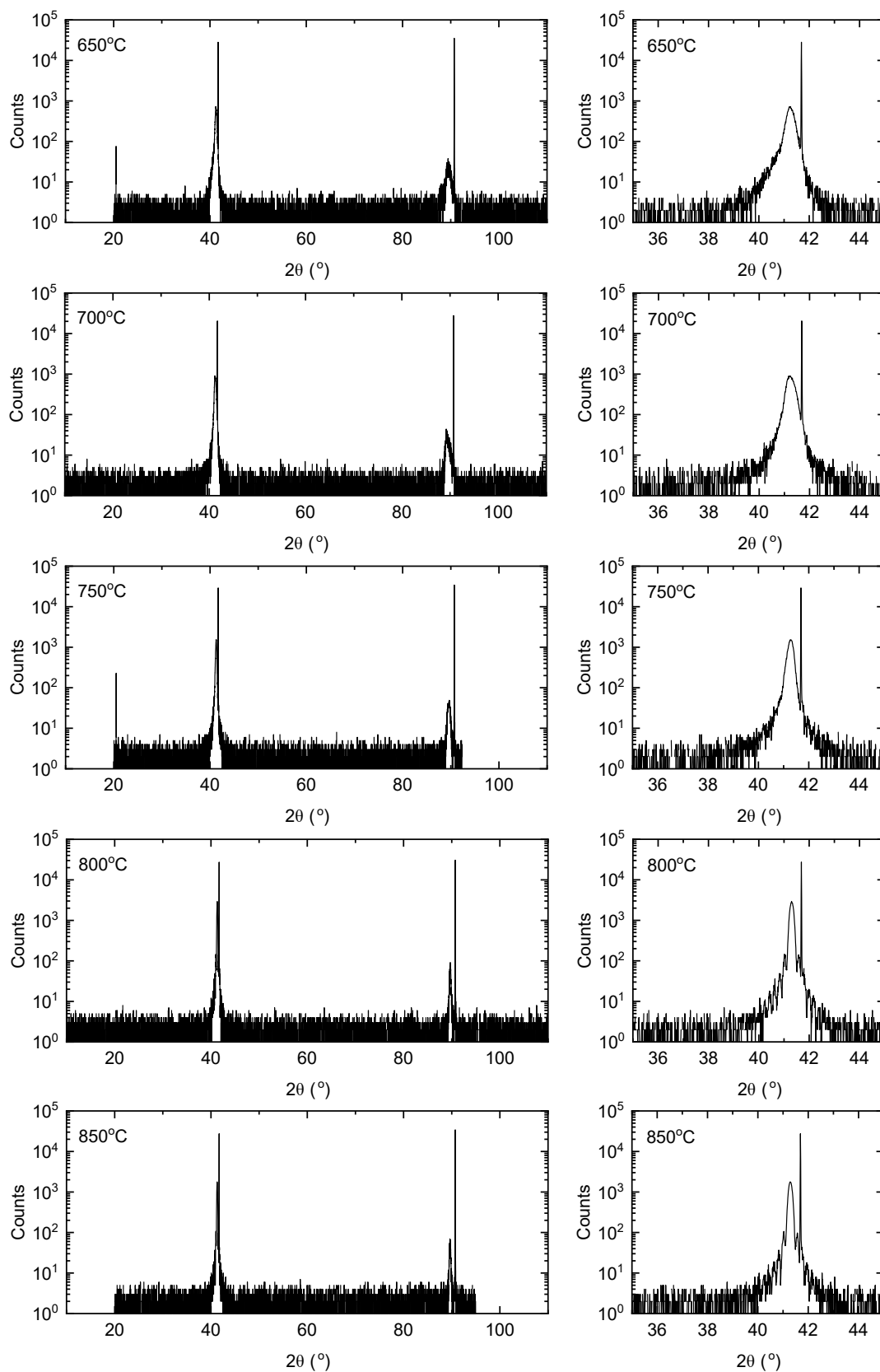


**Figure S3.** X-ray diffraction for the growth temperature set of samples reported in the main text. Left column: Full data range. Right column: Cropped region around the 111 structural peak.

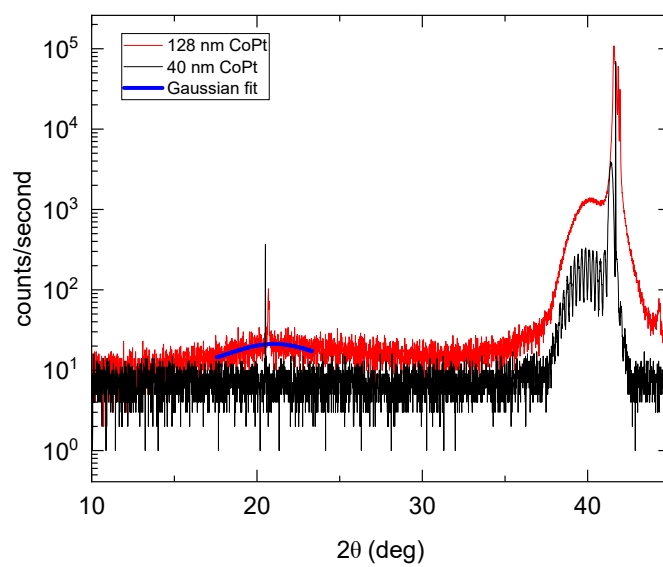


**Figure S4.** X-ray diffraction for the 350°C growth temperature over selected range. The 128 nm sample shows evidence of a superstructure peak at  $2\theta \approx 21^\circ$ .

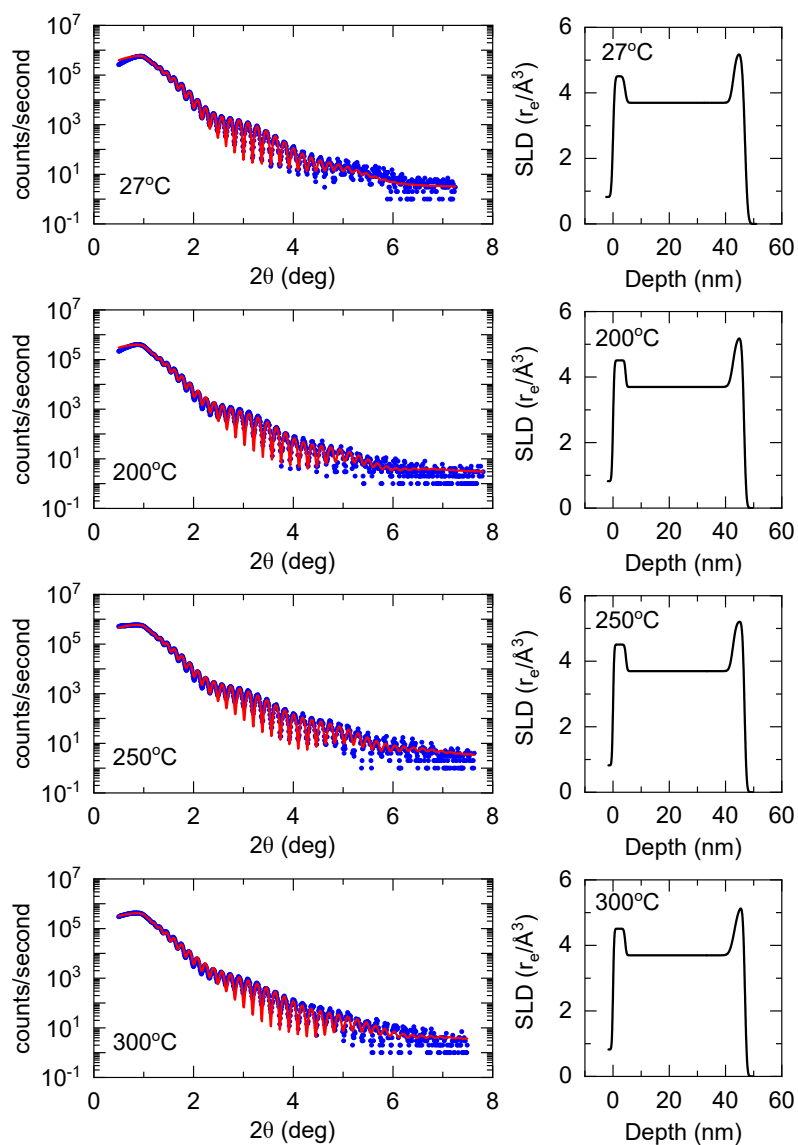


**Figure S5.** X-ray reflectivity for the growth temperature set of samples reported in the main text. Left column: Full data range with best fit line. Right column: Structural model corresponding to best fit.

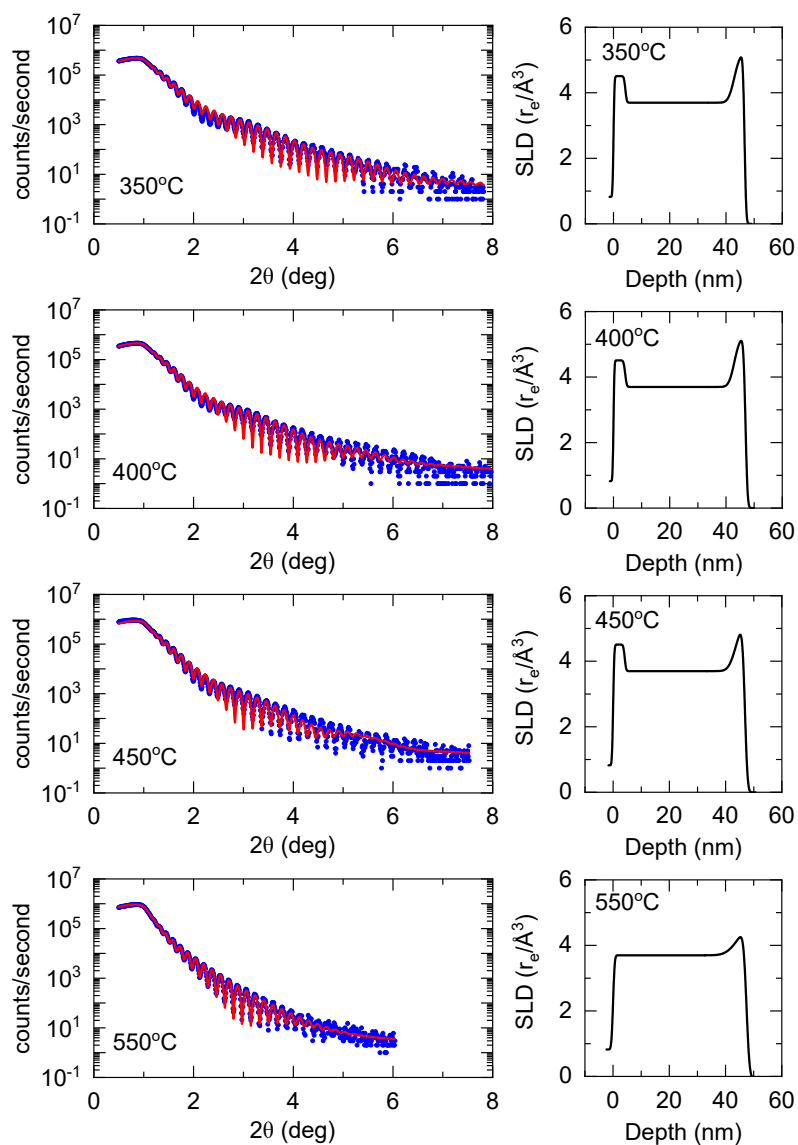


**Figure S6.** X-ray reflectivity for the growth temperature set of samples reported in the main text. Left column: Full data range with best fit line. Right column: Structural model corresponding to best fit.

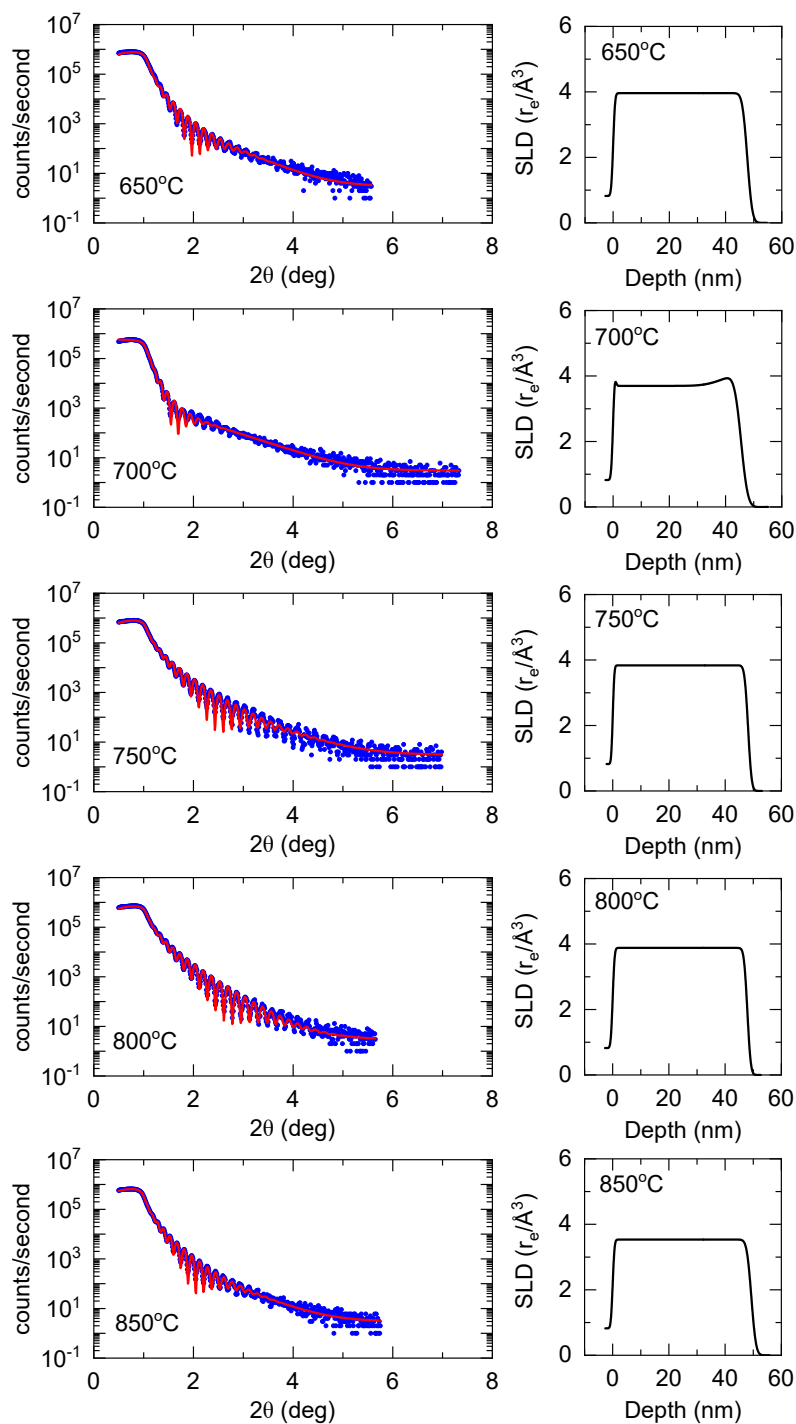


**Figure S7.** X-ray reflectivity for the growth temperature set of samples reported in the main text. Left column: Full data range with best fit line. Right column: Structural model corresponding to best fit.

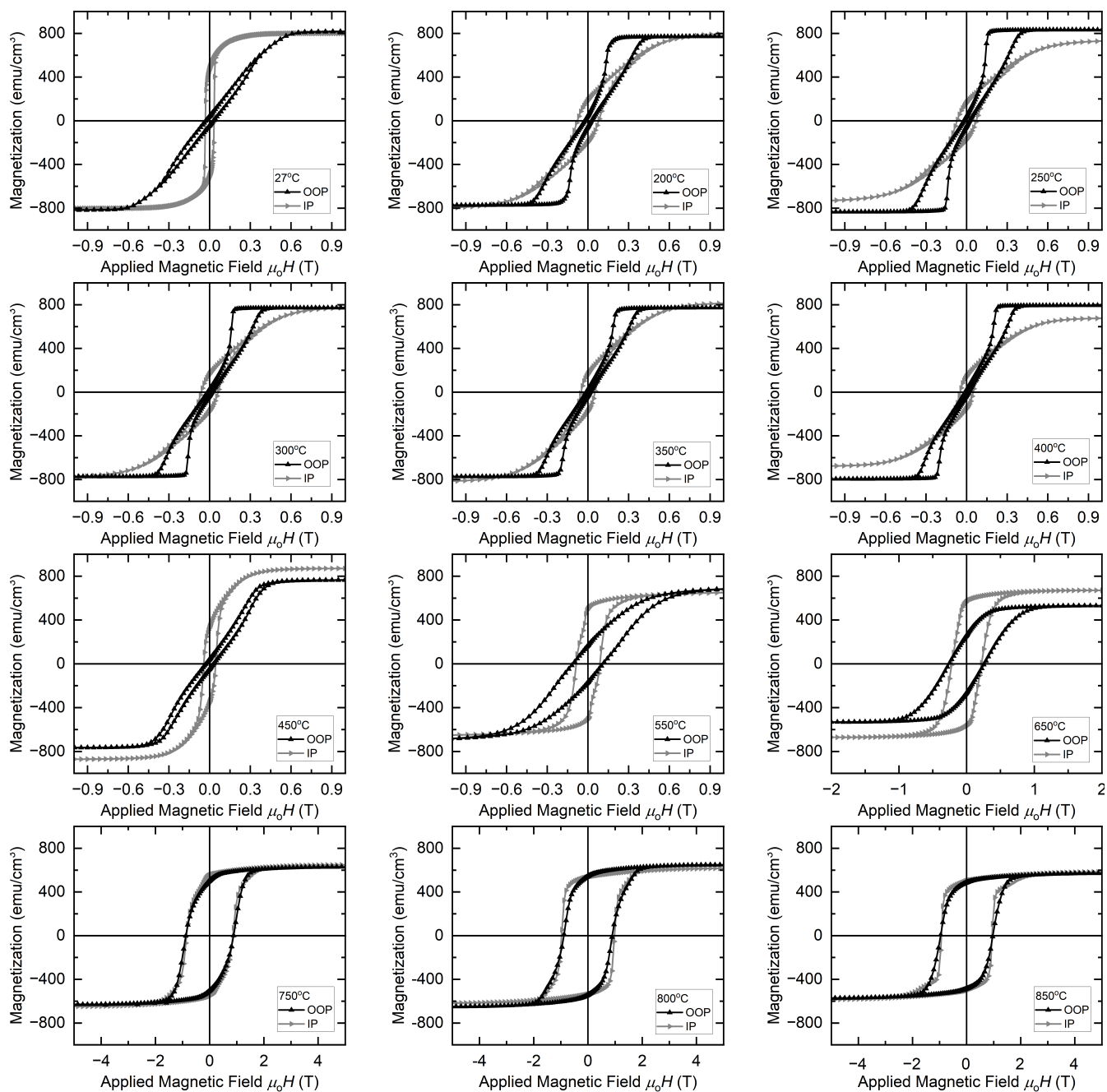


**Figure S8.** Volume magnetisation for the growth temperature set of samples reported in the main text. The thickness of all samples is 40 nm.



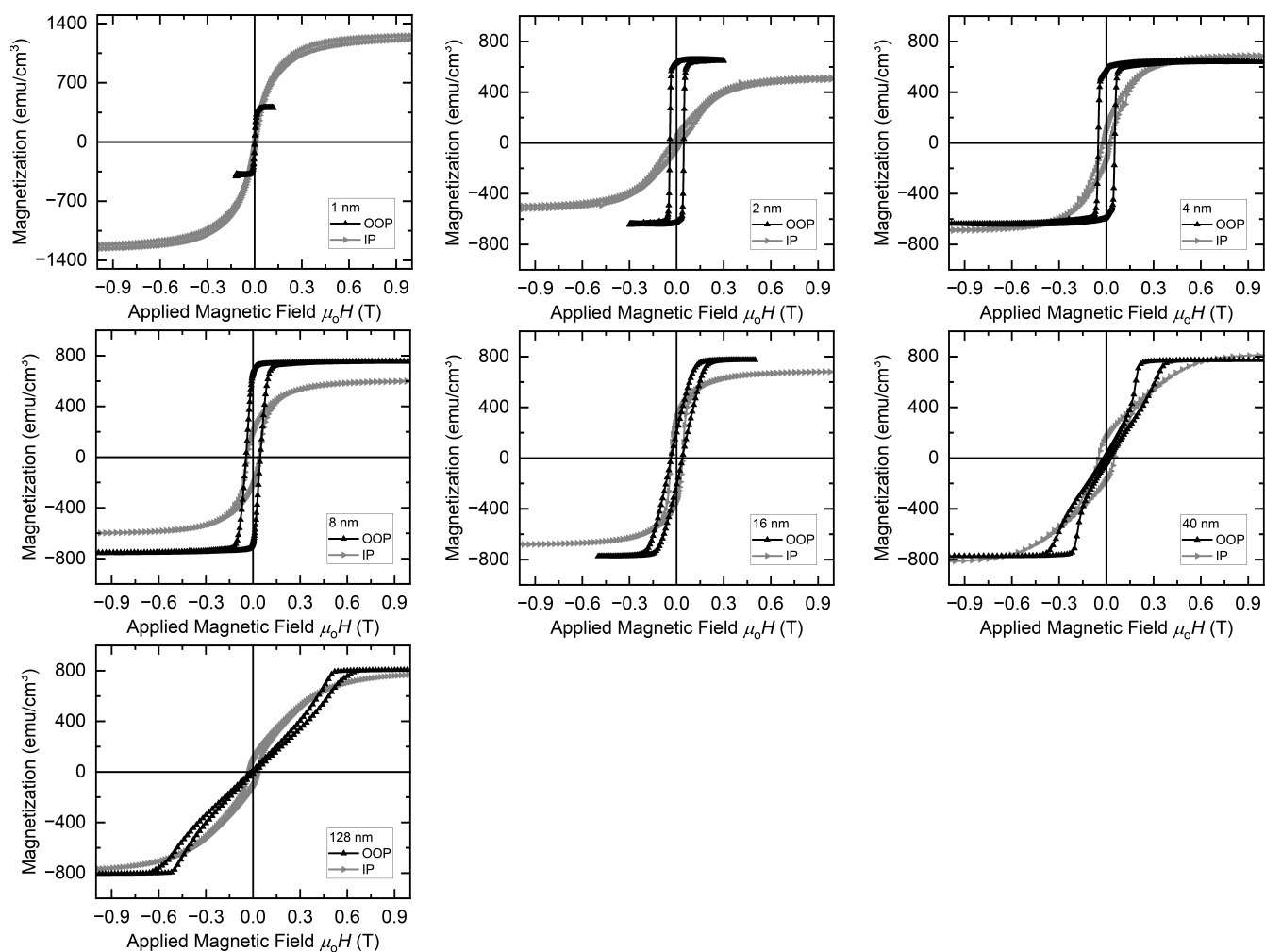


**Figure S9.** Volume magnetisation for the thickness series set of samples reported in the main text for growth at 350°C.

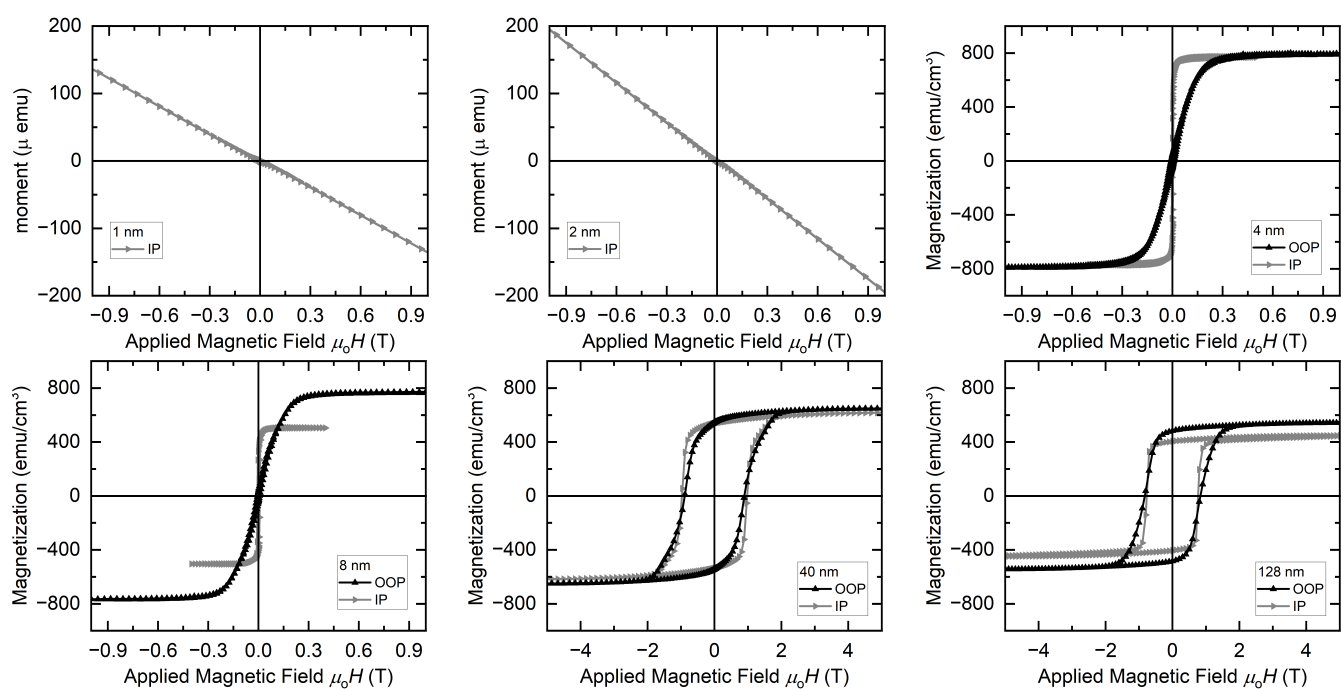


**Figure S10.** Volume magnetisation for the thickness series set of samples reported in the main text for growth at 800°C. For the 1 nm and 2 nm samples which did not show ferromagnetism, the uncorrected moment vs field is presented.